# Geomechanical Modeling of Ground Surface Deformation Associated with Thrust and Reverse-Fault Earthquakes: A Distinct Element Approach

Kristen Chiama\*<sup>1</sup>, Benjamin Chauvin<sup>1,2</sup>, Andreas Plesch<sup>1</sup>, Robb Moss<sup>3</sup>, and John H. Shaw<sup>1</sup>

# ABSTRACT -

We seek to improve our understanding of the physical processes that control the style, distribution, and intensity of ground surface ruptures on thrust and reverse faults during large earthquakes. Our study combines insights from coseismic ground surface ruptures in historic earthquakes and patterns of deformation in analog sandbox fault experiments to inform the development of a suite of geomechanical models based on the distinct element method (DEM). We explore how model parameters related to fault geometry and sediment properties control ground deformation characteristics such as scarp height, width, dip, and patterns of secondary folding and fracturing. DEM is well suited to this investigation because it can effectively model the geologic processes of faulting at depth in cohesive rocks, as well as the granular mechanics of soil and sediment deformation in the shallow subsurface. Our results show that localized fault scarps are most prominent in cases with strong sediment on steeply dipping faults, whereas broader deformation is prominent in weaker sediment on shallowly dipping faults. Based on insights from 45 experiments, the key parameters that influence scarp morphology include the amount of accumulated slip on a fault, the fault dip, and the sediment strength. We propose a fault scarp classification system that describes the general patterns of surface deformation observed in natural settings and reproduced in our models, including monoclinal, pressure ridge, and simple scarps. Each fault scarp type is often modified by hanging-wall collapse. These results can help to guide both deterministic and probabilistic assessment in fault displacement hazard analysis.

#### **KEY POINTS**

- Thrust fault ruptures produce complex surface deformation and hazards that are difficult to forecast.
- Distinct element method (DEM) models reproduce rupture patterns observed in analog experiments and natural settings.
- Models quantify patterns between fault displacement and ground deformation, supporting hazard estimates.

**Supplemental Material** 

# **INTRODUCTION**

In this study, we develop a mechanical basis for examining ground surface deformation that occurs during large thrust and reverse-fault earthquakes. Active thrust faults pose significant earthquake hazards at convergent plate boundaries around the world. Events such as the 1988 M 6.9 Spitak, Armenia, 1999 M 7.6 Chi-Chi, Taiwan, 2008 M 7.9 Wenchuan, China, 2013

M 7.2 Bohol, Philippines, and 2016 M 7.8 Kaikoura, New Zealand, earthquakes, demonstrate the complex nature of these ruptures, which often exhibit significant components of coseismic folding, secondary faulting, and distributed fracturing (Philip *et al.*, 1992; Kelson *et al.*, 2001; Wesnousky, 2008; Hubbard and Shaw, 2009; Xu *et al.*, 2009; Chang *et al.*, 2015; Kaiser *et al.*, 2017; Boncio *et al.*, 2018; Litchfield *et al.*, 2018; Bray *et al.*, 2019; Rimando *et al.*, 2019). Patterns of deformation

Cite this article as Chiama, K., B. Chauvin, A. Plesch, R. Moss, and J. H. Shaw (2023). Geomechanical Modeling of Ground Surface Deformation Associated with Thrust and Reverse-Fault Earthquakes: A Distinct Element Approach, *Bull. Seismol. Soc. Am.* 113, 1702–1723, doi: 10.1785/0120220264

© Seismological Society of America

<sup>1.</sup> Department of Earth and Planetary Sciences, Harvard University, Cambridge Massachusetts, U.S.A., https://orcid.org/0000-0002-0229-1177 (KC); https://orcid.org/0000-0002-6495-3551 (BC); https://orcid.org/0000-0002-3355-9199 (AP); https://orcid.org/0000-0002-3971-3812 (JHS); 2. Now at Mira Geoscience Ltd., Westmount, Quebec, Canada; 3. Department of Civil and Environmental Engineering, California Polytechnic State University, San Luis Obispo, California, U.S.A., https://orcid.org/0000-0003-1104-1476 (RM)

<sup>\*</sup>Corresponding author: kchiama@g.harvard.edu

(a) 1999 M 7.6 Chi-Chi, Taiwan



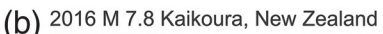




**Figure 1.** Images of ground surface deformation associated with coseismic thrust and reverse-fault displacements: (a) 1999 M 7.6 Chi-Chi, Taiwan, earthquake (photograph by W. J. Huang, reprinted with permission from fig. 1 in Chang *et al.*, 2015); and (b) 2016 M 7.8 Kaikoura, New Zealand, earthquake (photograph by Clayton Lindstrom 15 November 2016 in Bayer, 2017).

at or near the ground surface (Fig. 1) pose specific hazards when earthquakes occur in urban environments and impact critical information systems, energy transmission infrastructure, and transportation systems (Kelson et al., 2001; Petersen et al., 2011; Chang et al., 2015; Boncio et al., 2018; Bray et al., 2019; Baize et al., 2020). The displacement magnitude, width, and degree of tilting or warping of the ground surface associated with fault traces have an important impact on the ability of built structures to withstand these earthquakes (Kelson et al., 2001; Petersen et al., 2011; Boncio et al., 2018). For example, the Trans-Alaskan pipeline was built in the mid-1970s to withstand potential slip on the Denali fault based on initial fault displacement hazard estimates (Sorensen and Meyer, 2003). When the Denali fault ruptured in the 2002 M 7.9 earthquake, the pipeline withstood 5.5 m of right-lateral strike-slip offset demonstrating how fault displacement hazard assessments can successfully aid in the design of sensitive infrastructure and facilities (Cluff et al., 2003; Sorensen and Meyer, 2003; Nyman et al., 2014). However, building and retrofitting such facilities often requires an ability to forecast specific characteristics of future ground surface deformation related to individual faults—a capability that we generally lack (Moss and Ross, 2011; Petersen et al., 2011; Chang et al., 2015; Moss et al., 2018).

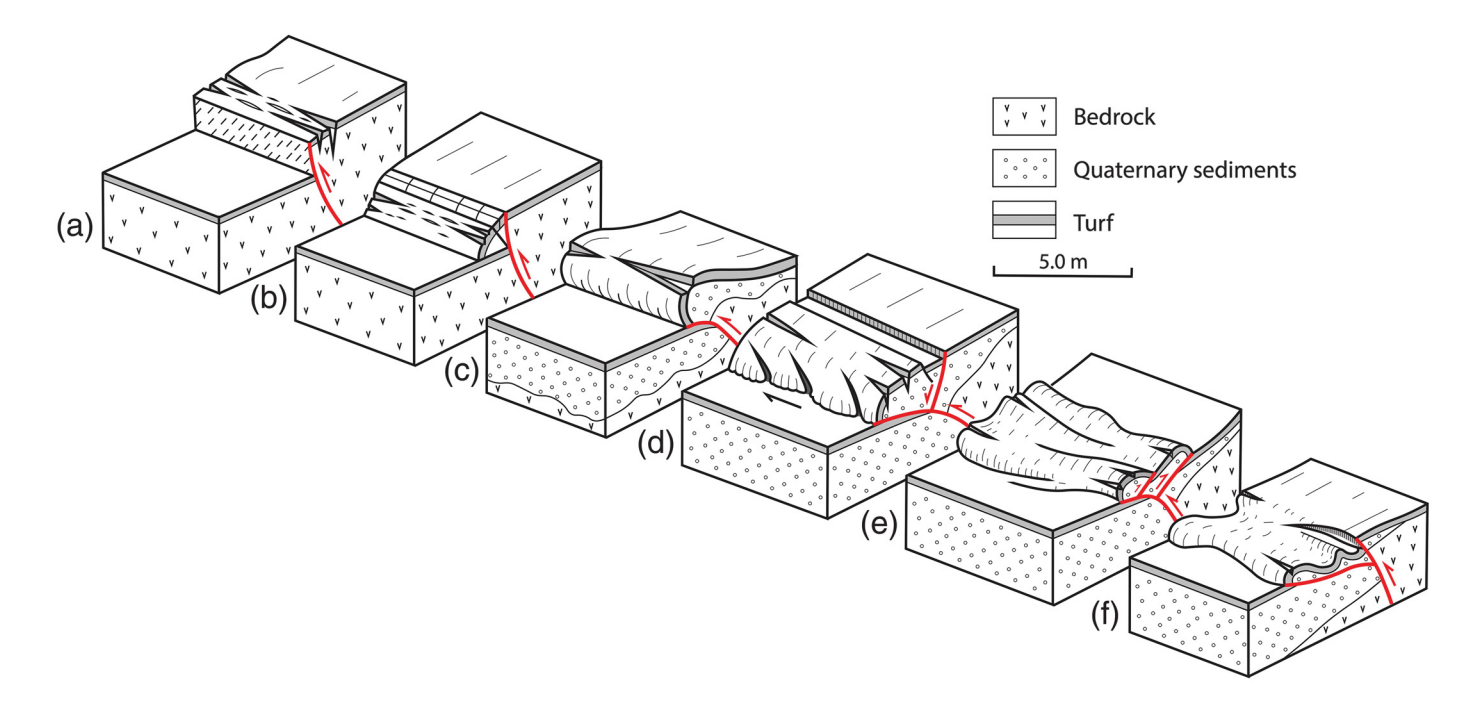
Large earthquakes produce a range of hazards, including strong ground shaking, liquefaction, trigger landslides, and tsunamis. Strong ground shaking is generally considered the most impactful of these hazards for onshore earthquakes because it affects large areas—often far from the earthquake epicenter. However, surface displacements along fault zones—the most direct result of earthquake ruptures—also pose serious hazards due to the intense damage that typically occurs to buildings and other structures that lie along the fault traces. Events such as the 1999 M 7.6 Chi-Chi, Taiwan, and 2008 M 7.9 Wenchuan, China, earthquakes demonstrate these risks because the most severe damage and the greatest loss of life resulted from the collapse of buildings along the fault rupture (Kelson *et al.*, 2001;

Hubbard and Shaw, 2009; Xu *et al.*, 2009; Boncio *et al.*, 2018; Ran *et al.*, 2019; Hughes, 2020).

Patterns of ground surface deformation are regularly studied in the field after large earthquakes, as well as through paleoseismic trenches that seek to define past earthquake behavior (Kelson *et al.*, 2001; Chen *et al.*, 2007; Ran *et al.*, 2019; Rimando *et al.*, 2019; Baize *et al.*, 2020). Postearthquake field surveys, combined with modern techniques such as light detection and ranging, are pro-

viding unprecedented details about the nature and complexity of this deformation (Stockmeyer et al., 2014; Bray et al., 2019; Rimando et al., 2019; Baize et al., 2020). Fault displacement hazard analysis (FDHA) is the primary method by which quantification of hazards associated with ground surface rupture is determined (Youngs et al., 2003; Moss and Ross, 2011; Petersen et al., 2011; Baize et al., 2020). FDHA provides an estimate of the potential amount of displacement on a fault during surface rupture based on statistical modeling of empirical data and, when available, a record of past earthquake ruptures. The majority of such studies have focused on strike-slip faults that have clearly defined fault traces and associated patterns of ground deformation (Petersen et al., 2011; Baize et al., 2020). Rupture traces and deformation patterns of thrust and reversefault events differ by nature. They are arguably more complex and far less well studied (Chang et al., 2015; Boncio et al., 2018; Garcia and Bray, 2018a). The complexity of these ruptures reflects the low dip of the faults, displacement that is highly variable along strike, and the tendency for folding, among other factors (Fig. 2; Philip et al., 1992; Yeats et al., 1997; Boncio et al., 2018; Rimando et al., 2019). The geometrical complexity of faults combined with the limited number of large continental thrust fault earthquakes makes it particularly difficult to forecast patterns of ground surface deformation based simply on empirical approaches (Youngs et al., 2003; Moss and Ross, 2011; Petersen et al., 2011; Boncio et al., 2018; Baize et al., 2020).

To investigate the patterns of ground surface deformation associated with thrust and reverse faults, we develop a suite of numerical models using the distinct element method (DEM) to evaluate the effect of different faulting parameters (e.g., fault dip and accumulation of slip) as well as sediment mechanics (e.g., cohesion and tensile strength). Our numerical models aim to provide a quantitative basis to relate observed ground deformational features with fault displacements at depth that can be linked to earthquake magnitudes. These relationships can help



to forecast patterns of ground surface deformation associated with large-magnitude thrust and reverse-fault earthquakes.

#### **METHODS**

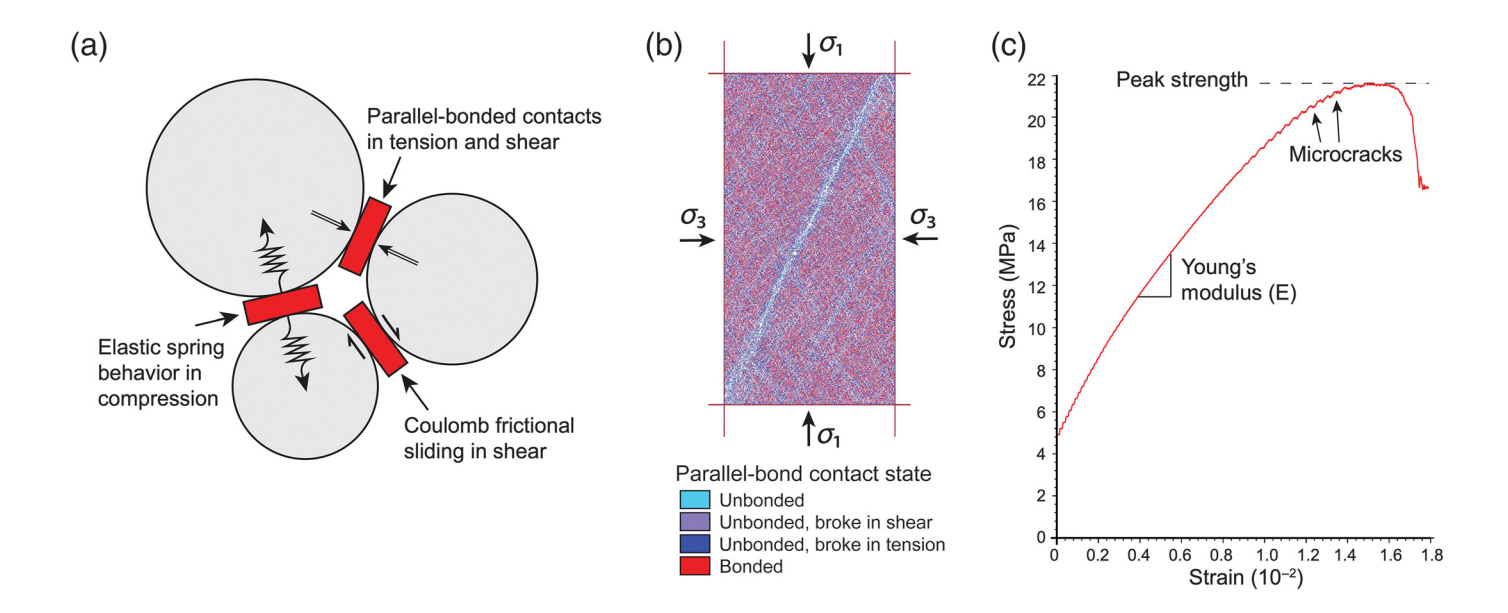
Structural geologists have long used mechanical models to investigate the processes of faulting and related folding over long deformation timescales. Models based on the discrete element method have proven very effective at reproducing the behavior of fault systems and the styles and kinematics of folding and associated deformation (Strayer and Hudleston, 1997; Finch et al., 2003; Imber et al., 2004; Strayer et al., 2004; Hardy and Finch, 2005, 2007; Benesh et al., 2007; Hughes et al., 2014; Hughes and Shaw, 2015; Hughes, 2020). These discontinuum methods define elastic and frictional particle interactions in aggregate materials exhibiting complex pseudoplastic behavior (Morgan, 1999; Guo and Morgan, 2004; Morgan, 2015). The invoked deformation processes are similar in many respects to how rocks and sediments are deformed in the upper crust and shallow subsurface (Morgan, 1999; Chang et al., 2015; Garcia and Bray, 2018b, 2019a,b). Moreover, these methods allow for the development of emergent structures, such as fractures, fissures, secondary, secondary faults, flexural slip surfaces, and folds (Erickson et al., 2001; Strayer and Suppe, 2002; Finch et al., 2003; Hardy and Finch, 2007; Hughes et al., 2014; Hughes and Shaw, 2015). The methods also facilitate the deposition, compaction, dilation, and deformation of sediments (Morgan, 1999; Guo and Morgan, 2004; Yang et al., 2006; Garcia and Bray, 2018b, 2019b). Recent work by Garcia and Bray (2018a, b) and Hughes (2020) compared DEM model results over a wide range of parameters (e.g., dense versus loose and strong versus weak sediment) to expected natural phenomenon in compressive regimes, thereby helping to establish relationships between modeled parameters and natural soil or sediment properties. The

**Figure 2.** Ground surface deformation along the Spitak fault from the 1988 M 6.9 Armenia, earthquake. The rupture had significant along-strike variations in surface deformation patterns, such as a (a) simple thrust scarp, (b) hanging-wall collapse scarp, (c) simple pressure ridge, (d) dextral pressure ridge, (e) backthrust pressure ridge, and (f) low-angle pressure ridge (adapted from fig. 4 of Philip *et al.*, 1992; Yeats *et al.*, 1997).

discrete element method, therefore, is well suited to model both the geologic processes of faulting and the granular mechanics of soil and sediment deformation in the shallow subsurface.

The discrete element method considers circular disks (2D) or solid spheres (3D) that are free to move relative to one another (Fig. 3). Once in contact, these disks, or particles, act as linear springs in compression and are governed by Coulomb frictional sliding in shear (Fig. 3). In addition, cohesive and tensile bonds (representing the shear and tensile strength, respectively) are applied at the contacts between particles through the parallel-bond contact model (Itasca, 1999, 2021). These bonds transmit force and only remain active until shear and tensional forces between the two particles reach prescribed limits (i.e., cohesion and tensile strength).

The discrete nature of this modeling method allows for strain localization and behavior that closely mimics natural deformation styles. Fractures, faults, and folds are all emergent features of these simulations that form due to displacement boundary conditions. Furthermore, the ability to set properties on a particle-by-particle basis allows modeling of anisotropic sequences of rocks or sediments (Hughes, 2020). In this way, we can examine how mechanical properties of the strata, such as layer thickness, cohesion, or vertical strength gradients, may affect the styles of ground surface deformation (Hughes *et al.*, 2014; Garcia and Bray, 2018a; Hughes, 2020).



A variety of DEM codes are readily available in the academic community, for example, cdem (Hardy and Cardozo, 2021), LIGGGHTS (Kloss et al., 2012), and Yade (Kozicki and Donzé, 2008). We employ Particle Flow Code (PFC2D version 6.00 and 7.00)—a commercial code based on the initial work of Cundall and Strack (1979) by Itasca (1999, 2021) that uses the "distinct" element method (within the family of the "discrete" element method), which defines deformable contacts between rigid bodies in an explicit, time-dependent solution. The method was originally developed and applied to investigate granular mechanics and problems of a geotechnical nature (Mustoe et al., 1987). The method has been adapted for geophysical and geological studies over a range of scales, including the evolution of fault gouge development in sheared fault zones (Mora and Place, 1998, 1999; Morgan, 1999, 2004; Morgan and Boettcher, 1999; Guo and Morgan, 2004), thin-skinned thrustfault evolution (Strayer and Suppe, 2002; Strayer et al., 2004; Benesh et al., 2007), extensional faulting and folding (Finch et al., 2004), and gravitational collapse of volcanic edifices (Morgan and McGovern, 2005a,b). Efforts to investigate faultrelated folding have focused on detachment folding (Hardy and Finch, 2005), basement-involved thrust and fault-propagation folding (Strayer and Suppe, 2002; Finch et al., 2003; Hardy and Finch, 2006, 2007; Hughes et al., 2014; Hughes and Shaw, 2015), fault-bend folding (Erickson et al., 2001, 2004; Strayer et al., 2004; Benesh et al., 2007), as well as fold-and-thrust belt and accretionary wedge mechanics (Strayer et al., 2001; Naylor et al., 2005; Morgan, 2015).

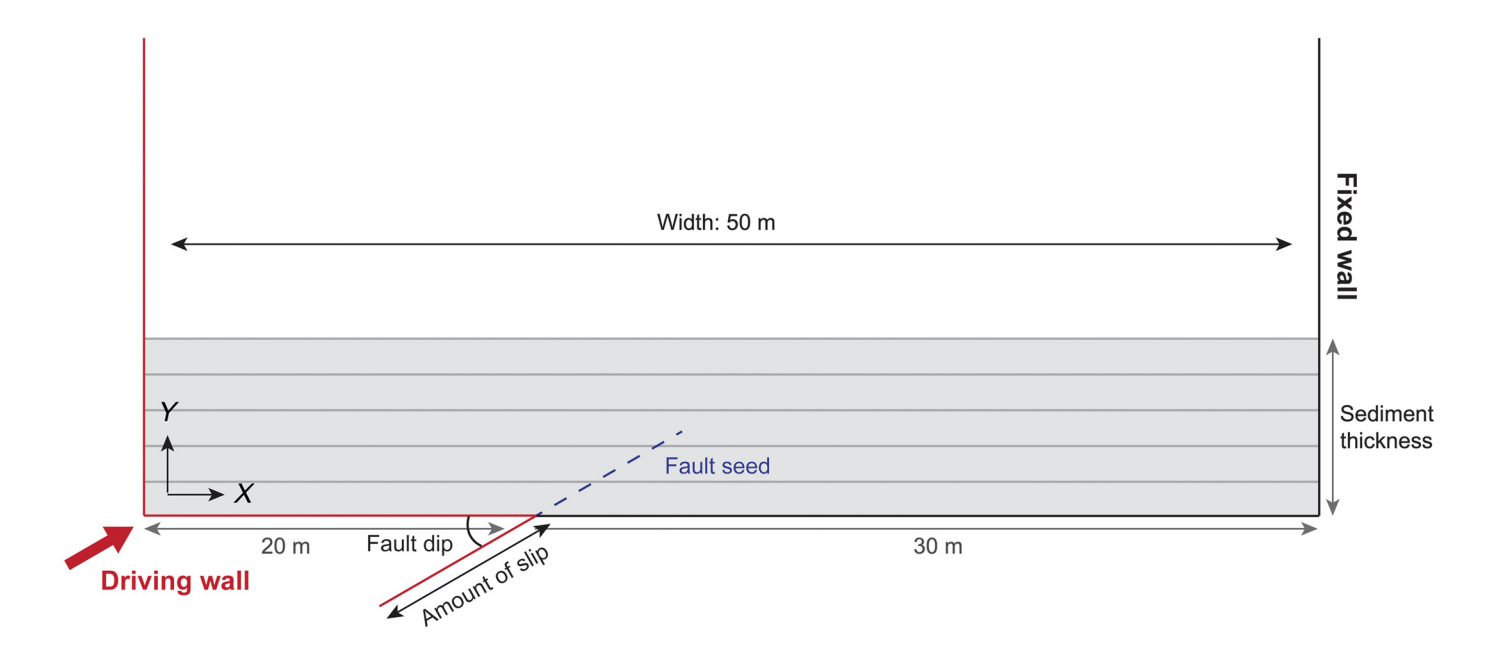
### **MODEL GEOMETRY AND FORMATION**

For our simulations, we employ a 2D model architecture with a discrete fault at depth that will displace and propagate upward into layers of sedimentary rocks and/or loosely consolidated sediments. This geometry is consistent with the natural settings we are investigating, in which thrust and reverse faults are

**Figure 3.** (a) An illustration of distinct element method (DEM) interparticle mechanics for the parallel-bond contact model adapted with permission from Hughes *et al.* (2014). (b) A biaxial stress test of numerically modeled dense material with  $2\times$  sand-sized, parallel-bonded particles with the contact-bond microproperties of cohesion and tensile strength set to 3.0 MPa. Bonded particles are indicated in red, bonds broken in tension are indicated in dark blue, bonds broken in shear are indicated in purple, and entirely unbonded particles are indicated in light blue. (c) The relationship of stress and strain from the biaxial stress test in panel (b) shows how the peak axial stress at failure (21.6 MPa) and Young's modulus (E; 12.98 MPa with an  $R^2$  value of 0.999) are obtained.

present at depth and propagate upward through near-surface sediment during large earthquakes. This basic model geometry has been applied in sandbox fault models as well as the previous numerical DEM simulations (Lade *et al.*, 1984; Hardy and Finch, 2007; Bransby *et al.*, 2008; Chang *et al.*, 2015; Garcia and Bray, 2018a). Our model is 50 m wide to simulate natural scales of deformation, has two vertical walls at either end, and has a thrust or reverse fault that initiates at the base of the model (Fig. 4). In PFC, we define faults using rigid, frictional walls. Much like particle-to-particle contacts, particles in contact with a wall are governed by Coulomb sliding in shear and subject to a linear restoring force in compression. The walls serve to contain the particles and drive displacement of the hanging wall, yielding fault slip and subsequent deformation within the model.

The sediment profile is produced by generating particles and gravitationally settling the assemblage until a stable equilibrium is reached (the mean unbalanced force is less than 1% of the total forces present in the model; Hughes, 2020). Particles are generated from a uniform box distribution (e.g., a rectangular distribution) of radii set by upper and lower bounds that define the maximum-to-minimum particle size ratio of  $\approx 2.5$ . This range of particle sizes prevents hexagonal close packing and associated



problems with predefined 60° planes of weakness (Finch et al., 2003; Strayer et al., 2004; Morgan and McGovern, 2005b). The initial interparticle friction coefficient ( $\mu_{int}$ ) is varied during gravitational settling to determine the density of particle packing. Low friction coefficients (0.0-0.2) yield dense particle assemblages, whereas high values yield loose assemblages (Garcia and Bray, 2018a). We focus on dense assemblages of material, as these best reproduce analog sandbox experiments and are shown to represent natural examples of fault scarp deformation in thrust and reverse-fault earthquakes. After reaching a stable equilibrium, the uppermost particles are removed to achieve a uniform thickness and flat topography. The particles rebound from the removal of this load and gravitationally settle to an equilibrium again before they are assigned to layers of uniform thickness (1.0 m). These "pregrowth" layers represent the uniform sedimentary strata prior to undergoing deformation.

Once the particles are generated and grouped into pregrowth layers, we modify the particle and contact parameters to define the sediment properties. The interparticle friction coefficient ( $\mu_f$ ) is reset to a standard value of 0.3 to generate realistic shear bandwidths during deformation (e.g., Morgan, 1999, 2004; Garcia and Bray, 2018a,b). We tested a range of values around  $\mu_f = 0.3$  and determined that results are not sensitive to the friction coefficient unless extreme values are used, consistent with findings of other authors (e.g., Morgan, 1999, 2004). The particles are then assigned stiffness, cohesion, and tensile strength values through the parallel-bonded contact model (described in the Sediment Mechanics Calibration section) and allowed to gravitationally settle, which yields a layered stratigraphy (Itasca, 1999; Strayer et al., 2004; Hardy and Finch, 2005; Hughes, 2020). To investigate the effects of sediment strength on the fault propagation and ground surface rupture, we simulate a range of homogeneous sequences (from strong to weak) by modifying the cohesion and tensile strength of the contact bonds.

**Figure 4.** Illustration of the 2D model for our DEM fault simulations (not to scale). Sedimentary units (pregrowth) are deposited horizontally. Deformation is driven by displacement of the driving wall (representing the hanging wall) parallel to the fault surface.

Once the sediment is generated and bonded, we begin the deformation sequence. Deformation is driven by displacement (Dirichlet) boundary conditions of the hanging-wall parallel to the fault at depth (Fig. 4). The amount of slip is defined as the total displacement at the base of the model and is run from 0 m to the maximum prescribed amount continuously. Thus, we can interrogate the model after any amount of slip (e.g., 2.0 m) to determine the geometry of the fault as it propagates to the surface and evaluate the associated ground surface characteristics. Once the model reaches the prescribed total accumulation of slip on the fault, in this case 5.0 m, the particles undergo continued gravitational settling to reach a stable equilibrium; this would be similar to a fault scarp settling due to gravity after the abrupt motion of the earthquake.

Displacement is calculated over distance intervals and time steps appropriate to reflect coseismic rupture. At each time step, Newton's equations of motion are solved by summing the forces on each particle, and then integrating to yield new velocities and positions (Itasca, 1999). As the simulation progresses, the energy of the system is reduced by the interparticle frictional resistance and through a dashpot-force damping coefficient of 0.70 (Cundall and Strack, 1979; Morgan, 1999, 2004; Finch *et al.*, 2003; Morgan and McGovern, 2005a,b; Hughes *et al.*, 2014; Garcia and Bray, 2018a,b). We evaluated a range of damping coefficient values in conjunction with hanging-wall displacement velocities and timesteps to avoid undesirable dynamic effects (e.g., particles flying upward at the onset of deformation), and selected values that yield stable, localized deformation within reasonable computational time.

TABLE 1

DEM Model Parameters and Biaxial Stress Test Results for the Sediment Assemblage

DEM Microproperties		Bulk Material Properties					
Contact Bond Cohesion (MPa)	Contact Bond Tensile Strength (MPa)	Young's Modulus (MPa)	R <sup>2</sup>	Peak Stress (MPa)	Failure Angle (θ°)	Friction Angle (φ°)	Friction Coefficient
0.1	0.1	8.83	0.999	12.71	62.0	34.0	0.68
0.5	0.5	11.99	0.999	13.73	63.5	37.0	0.75
1.0	1.0	14.02	0.993	14.21	60.0	30.0	0.58
1.5	1.5	16.72	0.998	14.55	60.0	30.0	0.58
2.0	2.0	17.43	0.999	14.90	61.0	32.0	0.63

DEM, distinct element method.

In addition, we implement a "fault seed" function prior to displacing the hanging wall. The fault seed propagates a plane of weakness at the specified fault dip into the sediment (Fig. 4). The length of the fault seed is a fraction of the total sediment thickness (25%, 50%, or 75%) such that it will have the same vertical thickness of sediment above the fault tip for different fault dips (e.g., 20° or 60°). Fault seed lengths of 25%, 50%, and 75% of 5.0 m thick sediment correspond to 3.75, 2.5, and 1.25 m of unruptured sediment above the fault tip, respectively. The application of this fault seed function avoids undesirable localization of shear bands at the boundary of the model. More importantly, this effectively represents cases in which prior earthquakes ruptured through sediments just below the Earth's surface. Thus, the application of the fault seed function over various lengths allows us to examine how the fault will propagate from depth through unconsolidated or loosely consolidated sediments in which prior earthquakes have not localized a discrete fault plane. This includes cases in which a fault defined by prior ruptures extends upward into recently deposited, unfaulted sediments. Furthermore, the application of this fault seed allows us to vary the amount of unruptured sediment above the fault tip without regenerating the total sediment depth for each experiment, thus saving significant computational time.

Additional details regarding the method and model parameters are provided in the supplemental material available to this article.

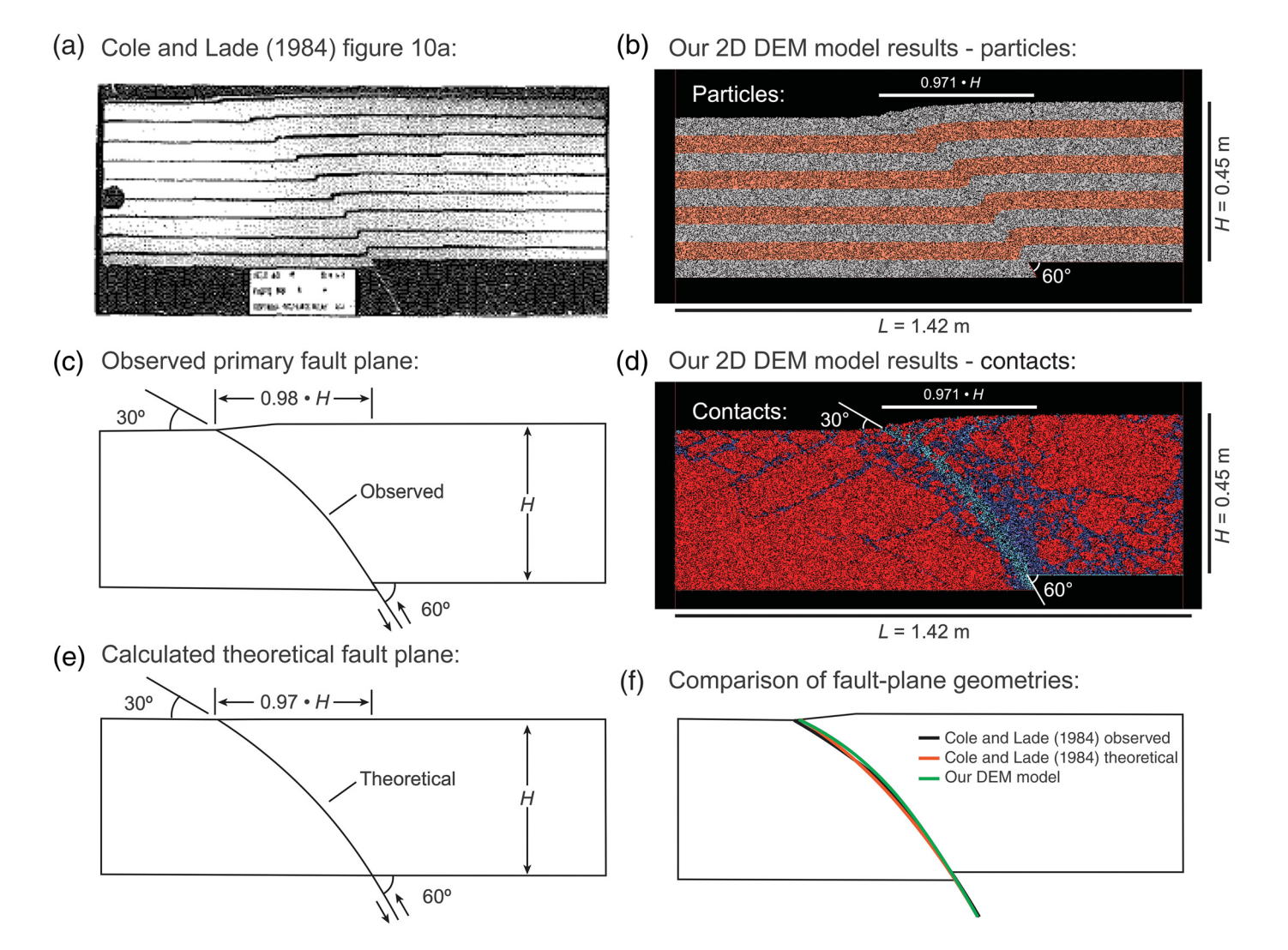
# **SEDIMENT MECHANICS CALIBRATION**

The generation of an initial particle configuration with either a uniform or stratified composition is a straightforward process; however, assigning specific bulk rock properties to a layer or interval is more difficult, owing to the particle-based nature of DEM. Microparameters are assigned to the individual particles that must be calibrated to ensure that the aggregate properties and characteristics are appropriate to natural phenomena (Morgan, 1999; Strayer *et al.*, 2004; Yang *et al.*, 2006; Hughes *et al.*, 2014; Chang *et al.*, 2015; Garcia and Bray, 2018b; Hughes, 2020). This calibration is accomplished by carrying out numerous quantitative, biaxial stress tests over a

range of confining stresses to obtain Young's modulus (elasticity; E) of the material (Itasca, 1999, 2021; Hughes *et al.*, 2014; Hughes, 2020; see Fig. 3b,c). The biaxial stress tests for the range of materials we are examining as near-surface sediment yield elastic values of 8.83-17.43 MPa and an average bulk friction coefficient of  $0.64 \pm 0.08$ , which falls within the range of laboratory measurements for rock and sediment specimens (Table 1; Jaeger and Cook, 1976). In addition to biaxial stress tests, we calibrated our material properties by replicating several reverse fault sandbox models such as Cole and Lade (1984) and Bransby *et al.* (2008), as well as the DEM models from Garcia and Bray (2018a). Based on these calibrations, we developed a set of experiments to demonstrate the capability of a DEM approach to explore how variations in key parameters influence observed ground surface deformation.

First, we present a DEM model that replicates the analog experiment presented by Cole and Lade (1984) and compare the observed fault-plane geometries in Figure 5. The DEM model depicts both the particles and contact bonds between particles such that broken bonds (blue) can be mapped to characterize internal deformation and define a geometry of the primary fault plane. The majority of slip in this model is consumed by motion along the primary fault plane (light blue broken contacts) with some minor, secondary fractures forming near the fault (dark blue broken contacts). Notably, the faultplane geometries between the analog sandbox fault model and the DEM model are remarkably similar, including the shared characteristics of the fault shallowing toward the surface of the model. The DEM model indicates highly localized deformation along the fault plane. A biaxial stress test of this material with the same mechanical properties yields a Young's modulus of 12.86 MPa within the values of unconsolidated, fine-grained, well-sorted sand (Strayer et al., 2004; Jaeger et al., 2007).

A critical element of our models is the contact laws that are employed to define particle-to-particle interactions. Recent work by Garcia and Bray (2018a) has shown that 3D DEM is able to effectively reproduce analog experiments of ground surface deformation related to thrust faulting (Bransby *et al.*, 2008; Fig. 6a,b). The 3D DEM models from Garcia and Bray (2018a) feature no particle bonds and represent loose sand in

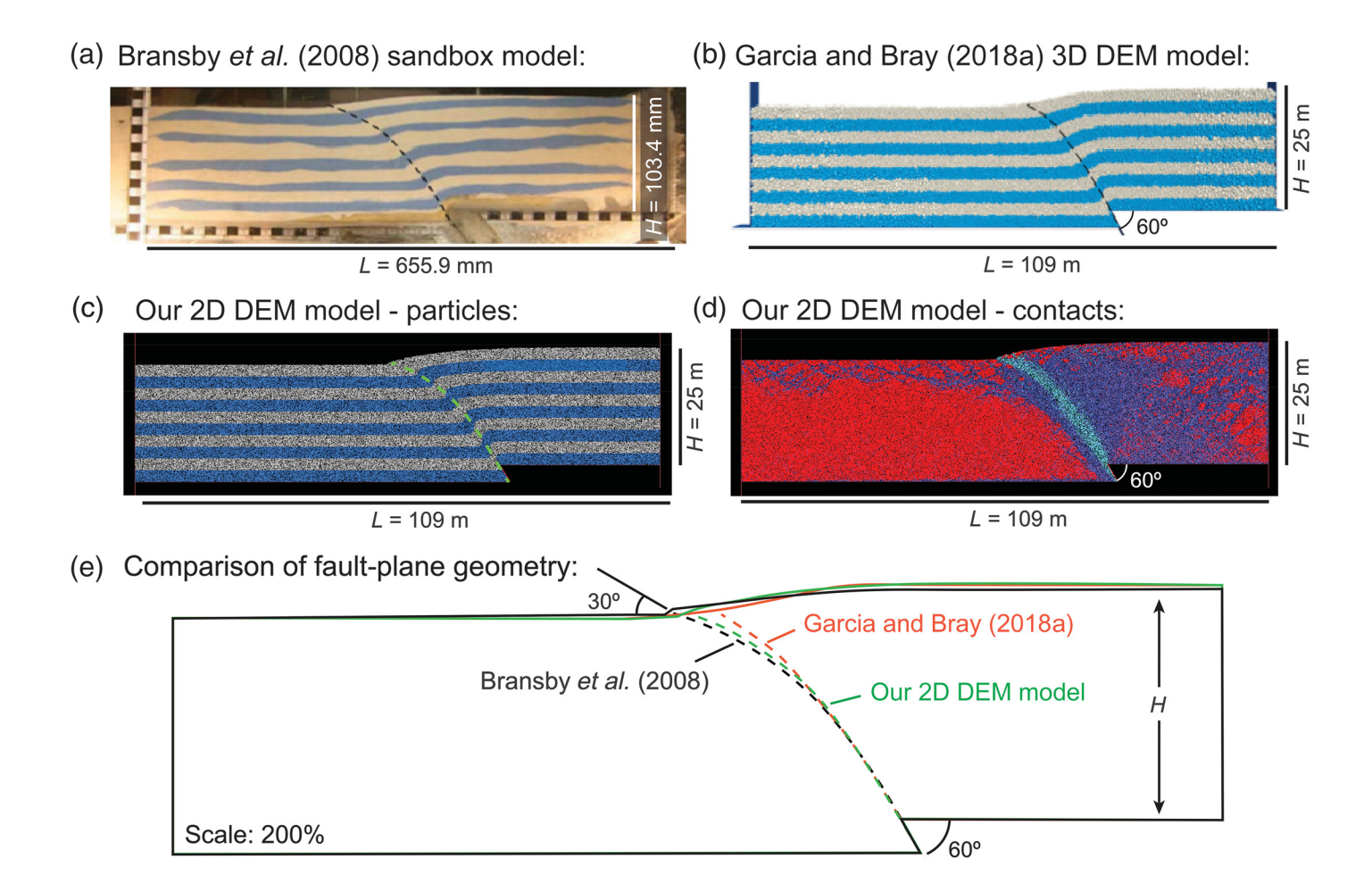


the linear contact-bond model with ideally spherical particles. To avoid excessive particle rotations, they employ a clustering approach that combines small group of particles together to represent angular grains. With this approach, their 3D models reproduce analog sandbox behavior because the third dimension and angular grains limit the rotation of the particles; however, these models are considerably time and computationally expensive. We implemented an alternative contact model that replicates realistic sediment mechanics using the parallel-bond contact model built-in to PFC. The parallel-bond contact model simulates a cement between particles that has a prescribed cohesion and tensile strength value over a set radius. This contact model sufficiently limits the excessive rotation of spherical particles (Itasca, 1999, 2021; Potyondy, 2011; see Fig. 3), similar to the effect of particle clustering employed by Garcia and Bray (2018a). Furthermore, this contact-bond model represents cohesive, frictional material that reproduces the physical properties observed in natural soils and sediments. A primary advantage of this contact-bond model is that it allows us to run large suites of 2D models with realistic particle dimensions in a computationally efficient manner. We tested a

**Figure 5.** Comparison of the (a) analog Cole and Lade (1984) sandbox fault model to (b,d) our 2D DEM model employing the same boundary conditions and sediment parameters with 2× sand-sized, parallel-bonded particles. The (a) analog sandbox fault model, (c) observed, and (e) theoretical fault-plane geometries presented in figure 10a of Cole and Lade (1984) are reproduced with permission on the left. The (b) sedimentary strata in the DEM model for a homogeneous sediment profile and the (d) contact bonds for the same model are shown subsequently. The red contacts are bonded particles, and blue represents broken contact bonds. See Figure 3 for a representative biaxial stress test of the simulated material. (f) The comparison between the observed and theoretical primary fault planes, as defined by Cole and Lade (1984) for a 60° dipping thrust fault, are remarkably similar to the primary fault-plane geometry in the DEM model result. Table S1 reports the parameters used in this model.

wide range of parameters to replicate analog (Cole and Lade, 1984; Bransby *et al.*, 2008) and 3D DEM models (Garcia and Bray, 2018a). This allowed us to calibrate the parameters used in our contact bonds to ensure that they effectively reproduce physically realistic behaviors observed in natural settings.

Second, we present a DEM model that replicates the analog experiment of Bransby et al. (2008), which was also reproduced



with a 3D DEM model by Garcia and Bray (2018a) (Fig. 6a,b). Our model (shown in Fig. 6c,d) uses largely the same sediment microproperties as the ones employed in the Cole and Lade (1984) replica. The primary fault planes and surface deformation of each model are strikingly similar with only a minor deviation in the location of the fault plane (Fig. 6e). The Garcia and Bray (2018a) fault-plane geometry is steeper than the reference analog model by Bransby et al. (2008). This is likely due to using a sediment assemblage that is less dense than an ideally packed matrix. Garcia and Bray (2018a) generated a loose sediment assemblage by increasing the initial interparticle friction coefficient ( $\mu_{\rm int}$ ) as the particles gravitationally settled (e.g., 0.5), and then reset this value to a standard 0.3 during the deformation sequence. The comparison of surface deformation profiles shows this difference in the assemblage density. The Bransby et al. (2008) profile has a sharp, steep fault scarp transition in which the fault plane intersects the surface (Fig. 6e). In contrast, the Garcia and Bray (2018a) surface profile has a shallow gradient and a smooth transition between the hanging-wall and footwall blocks (Fig. 6e). Meanwhile, our 2D DEM model used to replicate Bransby et al. (2008) has a frictional value of  $\mu_{\rm int} = 0.0$  during the gravitational settling of particles to create an ideally dense sediment assemblage. As noted previously, the interparticle friction coefficient ( $\mu_f$ ) is then set to 0.3 for the deformation sequence. This

**Figure 6.** Comparison of the (a) analog sandbox reverse fault model in Bransby *et al.* (2008) to the (b) 3D DEM replica in figure 5a from Garcia and Bray (2018a), which employed a clustering of particle shapes to limit the excessive rotation of spherical particles. (c,d) Our 2D DEM model applies the parallel-bond contact model that limits excessive particle rotations through cohesive bonds between particles that act as a cement between grains (Itasca, 1999). (e) A comparison of the primary fault-plane geometries reveals that our 2D DEM replica model is remarkably similar to the analog sandbox fault model results of Bransby *et al.* (2008). Table S2 reports the parameters used in this model.

localizes the deformation along a discrete fault plane that is slightly steeper than Bransby *et al.* (2008) but shallower than Garcia and Bray (2018a) (Fig. 6e). Overall, our 2D DEM replica model has a fault scarp that is similar in orientation and morphology to Bransby *et al.* (2008).

Our representation of the models in Bransby et al. (2008) and Garcia and Bray (2018a) demonstrates that the parallel-bond contact law used in our model is able to reproduce analog experiments, including dilatant granular and cohesive materials (Cole and Lade, 1984; Garcia and Bray, 2018a), by applying a cement between the particles. This enables us to evaluate a wide range of parameters in 2D simulations to comprehensively examine the natural processes influencing surface deformation in thrust and reverse-fault earthquakes.

# **RESULTS**

After calibrating our sediment mechanics and boundary conditions to analog models, we developed a series of DEM models that seek to define the key factors that control the style of ground surface rupture during thrust and reverse-fault earthquakes. We examined a series of parameters, including the amount of accumulated slip on a fault, the sediment strength mechanics, and the fault dip. We performed 45 experiments on dense, 5.0 m thick sediment in a model 50 m wide with a fault positioned 20 m from the driving wall and slipped each model at a constant rate (0.3 m/s) from 0 to 5.0 m continuously. We evaluated a wide range of sediment mechanics (cohesion and tensile strength: 0.1, 0.5, 1.0, 1.5, and 2.0 MPa) across 20°, 40°, and 60° fault dip angles with a fault tip buried by 3.75, 2.5, and 1.72 m of unruptured sediment corresponding to fault seed lengths of 25%, 50%, and 75% of the total sediment thickness, respectively. This section will present key results of these models with additional information on the methods and the complete model results provided in the supplemental material.

# INFLUENCE OF THE ACCUMULATION OF SLIP ON A FAULT

The primary influence on ground surface deformation from our models is the amount of slip accumulated on a fault at the base of the model. Figure 7 considers a homogenous stratigraphic sequence with sediment cohesion and tensile strength of 0.5 MPa above a fault that dips 40°. As the fault begins to slip, it propagates upward into the strata and is associated with internally distributed deformation in the form of secondary faulting and folding. As slip accumulates on the fault, the deformation zone width and vertical displacement increase. Furthermore, the fault tends to shallow as it approaches the surface after 2.0 m of slip (Fig. 7), consistent with the analog models from Cole and Lade (1984) and Bransby et al. (2008) (see Figs. 5 and 6). Ground surface deformation in our model is characterized by a discrete scarp that develops above the fault, with tilting of the ground surface and associated faulting that includes both thrust faulting and tensile fracturing. The deformation zone width and uplift both increase with additional hanging-wall displacement, achieving the maximum width of 11.2 and 3.2 m of uplift after 5.0 m of fault displacement. Meanwhile, the fault scarp dip increases to the maximum of 22° after 2.0 m of slip on the fault. At larger displacements (≥3.0 m) on faults dipping greater than 30°, the fault scarp is generally affected by mass wasting (hanging-wall collapse), and the scarp dip is limited to the angle of repose of the simulated colluvial wedge. As a result, the scarp dip begins to oscillate between steepening and shallowing to the angle of repose between stages of hanging-wall collapse.

# **INFLUENCE OF FAULT DIP**

The dip of the fault also has a major influence on the style of ground surface deformation. We compare models with 20°,

40°, and 60° dipping faults in moderate-strength sediment (1.0 MPa) after 2.0 m of accumulated slip in Figure 8. The 20° fault propagates upward into the sediments forming a broad zone of deformation (17.3 m) that is defined by the toe of the fault scarp and a pair of backthrusts (Fig. 8a,b). The 40° fault model has a smaller deformation zone width (7.3 m) and forms a tensile fracture at the crest of the scarp that will contribute to hanging-wall collapse after sufficient vertical displacement of the hanging wall is achieved (Fig. 8c,d). The 40° model develops a single dip panel with a scarp dip of 20°. The 60° fault model has the smallest deformation zone width (5.6 m), which is defined by the extent of a tensile fracture and the formation of a colluvial wedge (Fig. 8e,f).

We can identify relationships of fault scarp morphology based on the imposed fault dip angle from these models. The zone of deformation on shallower fault dips (20°) is larger than that on steeper faults (60°) for a similar amount of slip. Furthermore, low-angle faults, such as the 20° model, show a strong tendency to develop discrete high-angle fault splays and backthrusts within the deformation zone. The observed displacement and folding of sediments in Figure 8 reproduce many styles of surface scarps observed in nature (see Fig. 2e,f; Philip et al., 1992; Rimando et al., 2019). Moreover, the additional fault splays on shallow faults significantly increase the width of the overall deformation zone at the surface compared to the models of high-angle faults. Such differences could have major implications for the hazards associated with similar ruptures if they were to occur in densely urbanized environments or for pipelines or other transmission corridors that cross the fault trace. Together, these models illustrate how variations in fault dip have a major influence on the styles of ground surface deformation.

#### **INFLUENCE OF SEDIMENT STRENGTH MECHANICS**

Our suite of DEM models allows us to assess how variations in sediment strength influence surface rupture characteristics. In particular, the patterns of breakage in the bonds between particles (Figs. 7b and 8b,d,f) show how sediments of different strengths are affected by deformation. The contact bonds between particles are broken (indicated in blue in Figs. 7 and 8) in a zone associated with the up-dip projection of the fault as well as in the hanging wall in a zone that comprises the scarp. The relative motion of the particles drives contact bond breakage and the observed deformation patterns. We suggest that these areas of broken contacts reflect the granular mechanics of deformation that are appropriate to describe fault propagation through weak, loosely bonded, or unconsolidated sediments and are representative of shear bands (Garcia and Bray, 2018a). In many of our models, these features define zones of secondary fracturing and faulting (e.g., distinct splays), which are widely observed in the geomorphology of thrust and reverse-fault ruptures (Philip et al., 1992; Yeats et al., 1997; Boncio et al., 2018; Rimando et al., 2019).

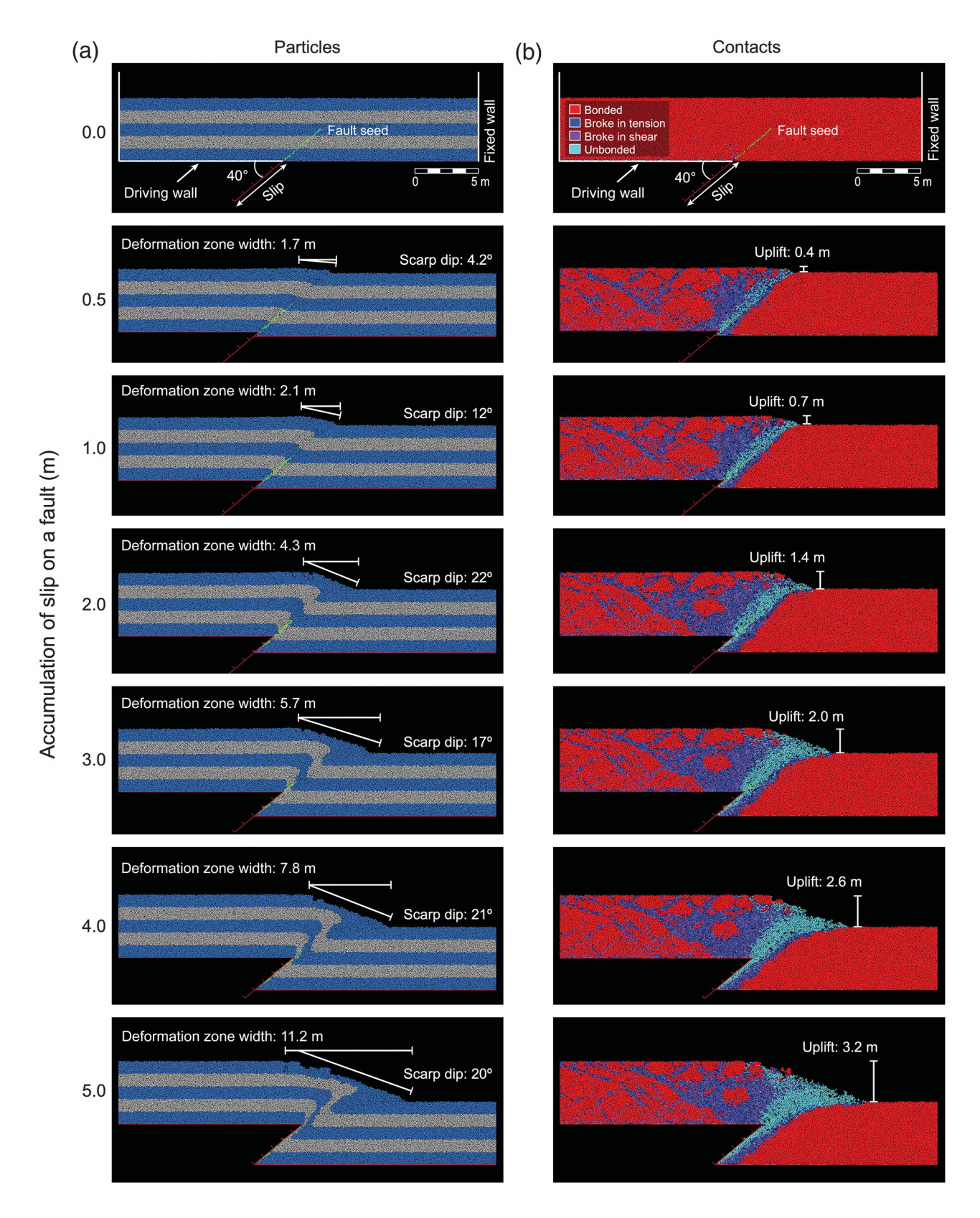
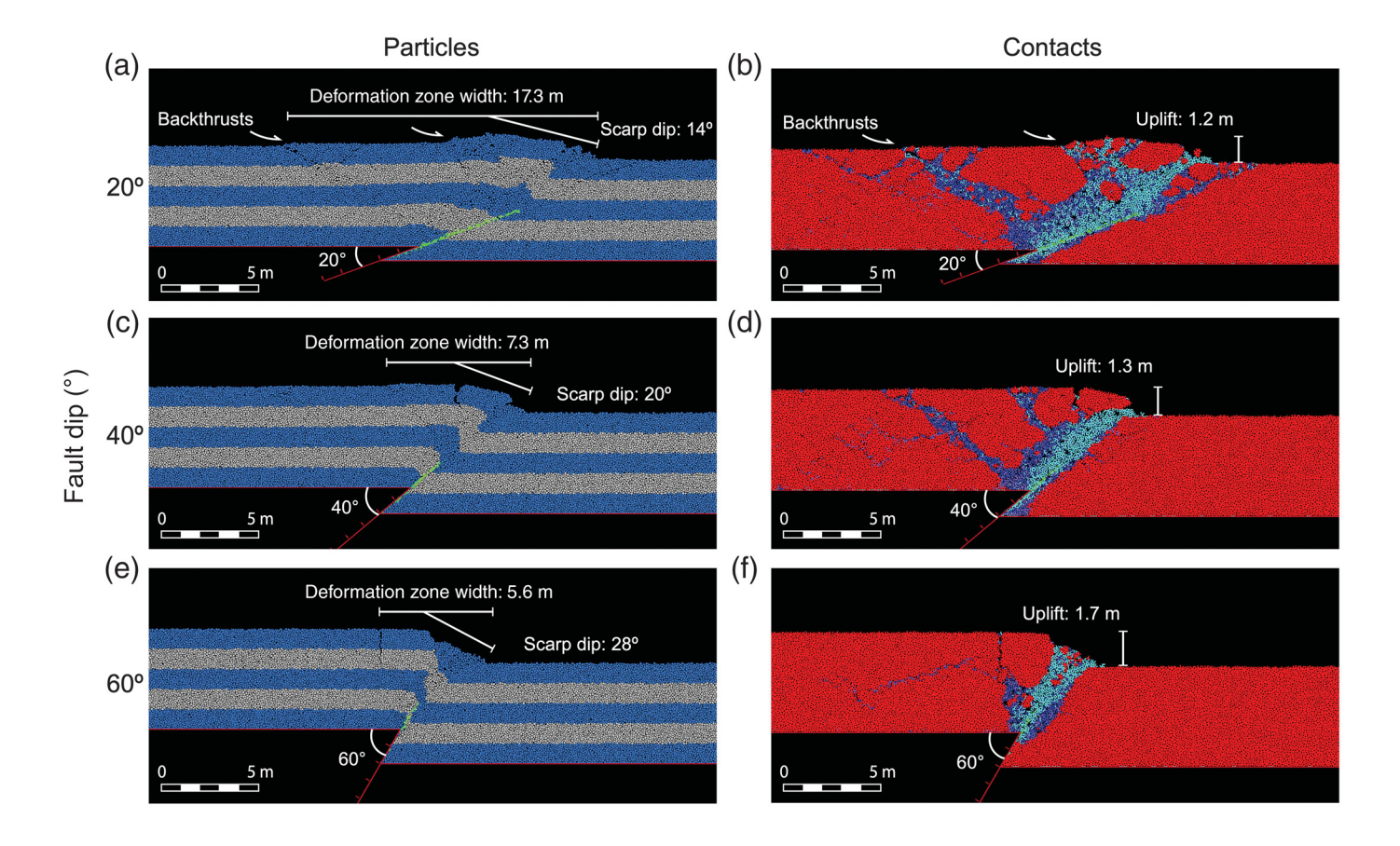


**Figure 7.** Sequential model showing increase in displacement and the resulting pattern of ground surface deformation. Deformation in the model is driven by displacement of the driving wall parallel to the fault surface. A fault seed is shown in green corresponding to 2.5 m of unruptured sediment above the fault tip. (a) Particles; and (b) contacts (red represents bonded particles and blue represents broken contact bonds). The panels depict an

increase in slip on a 40° fault from 0 m (top) to 5.0 m (bottom). The model is 50 m wide, has a particle density of 2600 kg/m², particle sizes of 0.025–0.06625 m (50× sand-sized), interparticle and fault friction coefficient of 0.3, sediment mechanics strength of 0.5 MPa, and a hanging-wall displacement velocity of 0.3 m/s. Table S3 reports the parameters used in this model.



Natural soils and strata have variable physical properties that can have an impact on styles of surface deformation related to fault rupture. Figure 9 illustrates how variations in the cohesion and tensile strength (0.1, 0.5, 1.0, 1.5, and 2.0 MPa) of the contact bonds between particles influence patterns of ground surface deformation across a range of fault dips (20°, 40°, and 60°) for experiments with 2.5 m of unruptured sediment above the fault tip. The additional 30 trials with variable thicknesses of sediment above the fault tip are provided in Figures S2 and S3.

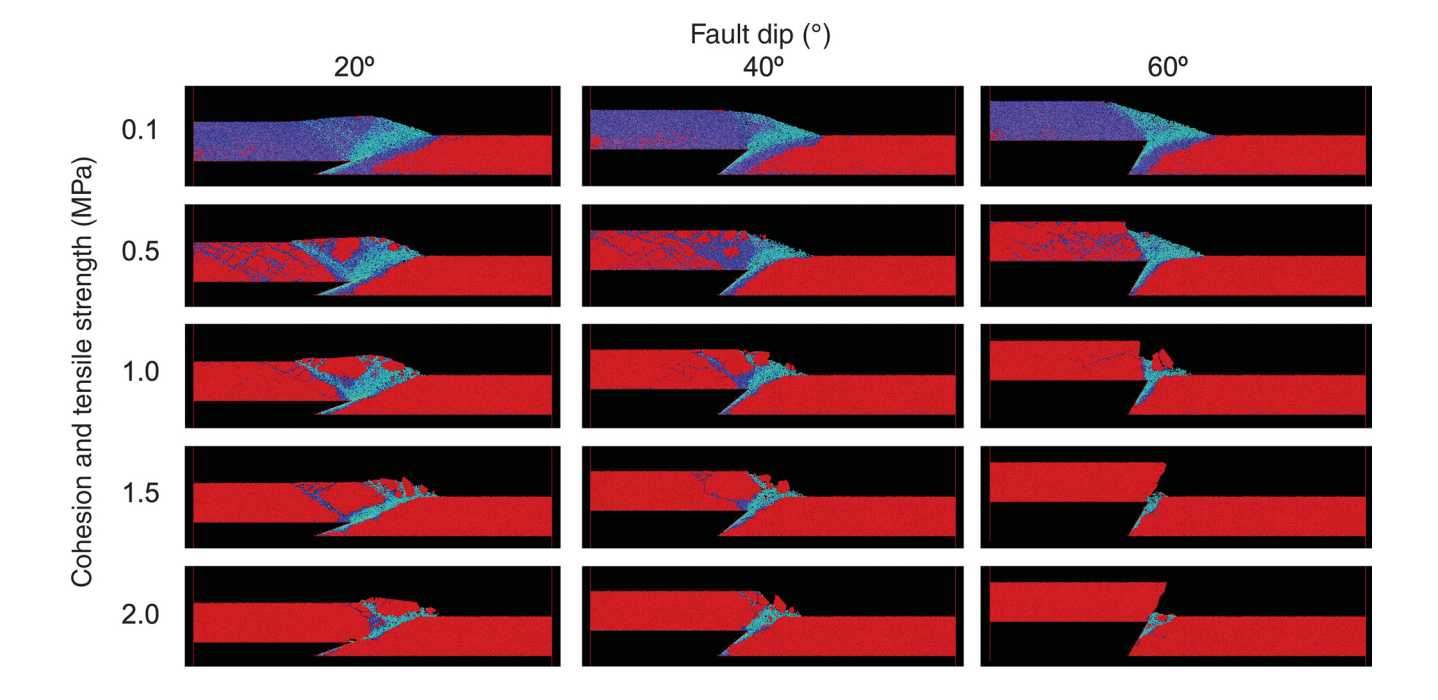
The variation of cohesion and tensile strength across similar fault dip angles show some similar characteristics of the fault zone; however, the degree of localization of the deformation varies considerably. Lower sediment strengths yield broadly distributed deformation with many broken bonds (indicated in blue in Fig. 9), whereas higher sediment strength mechanics localize the area of broken bonds to a narrow zone above the fault tip. The experiments depict the primary fault plane in light blue in which all contact bonds are broken and the particles can rotate freely. This contrast in strength is directly manifested in the pattern of ground surface deformation, in which the low strengths yield a broadly distributed zone of folding, tilting, and relatively shallow fault scarp dips. In comparison, higher strengths show narrow, steeply dipping scarps with more localized deformation throughout the hanging wall. In cases in which tensile fractures develop at the crest of the scarp, a colluvial wedge forms by hanging-wall collapse. Alternatively,

**Figure 8.** Comparison of models with different fault dips: (a,b) 20°; (c,d) 40°; and (e,f) 60° resulting in different styles of deformation in 1.0 MPa sediment after 2.0 m of slip on a fault. (a,c,e) Particles; (b,d,f) contact bonds (red indicates bonded and blue indicates broken bonds). Table S3 reports the parameters used in this model.

if the sediment is sufficiently strong to resist hanging-wall collapse on the 60° fault dips, a direct fault displacement (or overhang) can be observed. Thus, this matrix of experiment results in Figure 9 illustrates the influence of sediment strength and fault dip on the width and degree of tilting within the surface scarp, which has a primary influence on hazard.

To highlight these variations in ground rupture patterns, we compiled the surface deformation profiles for 36 experiments of shallow (20°), moderate (40°), and steep (60°) fault dips in weak (0.1 and 0.5 MPa cohesion and tensile strength) and strong (1.5–2.0 MPa cohesion and tensile strength) sediment in Figure 10. These experiments each accumulated 5.0 m of slip in dense, 5.0 m thick sediment for cases with 1.25, 2.5, and 3.75 m of unruptured sediment above the fault tip.

The shallow fault dip  $(20^\circ)$  experiments in weak sediment feature a wide zone of deformation (up to  $\sim 18.5$  m) defined by a shallow fault scarp  $(16.6^\circ)$  with a folded and uplifted panel in the hanging wall (Fig. 10a). In contrast, shallow fault experiments in strong sediment yield localized, brittle deformation with a backthrust in the hanging wall, a deformation zone



 $\sim$ 16.2 m wide, and blocks of simulated colluvium that collapse into the toe of the fault scarp, which steepen the fault scarp dip ( $\sim$ 24.4°; Fig. 10b). Both the sets of experiments exhibit a wide deformation zone bounded by folding or a backthrust that leads to a broad zone of uplift in the hanging-wall block (Fig. 10a,b).

Moderate and steep fault dips feature different characteristics of morphology. The moderate dipping faults (40°) in weak sediment have a deformation zone width defined by the extent of the colluvial wedge (~11.3 m) formed through a triangular wedge of distributed shear and an average scarp dip of 20.8° (Fig. 10c). The moderate fault dips in strong sediment (Fig. 10d) have more complex scarp morphologies dependent on the amount of sediment present above the fault tip (i.e., fault seed lengths). This range of morphologies includes two experiments presenting a backthrust, three experiments in which the colluvial wedge is dominated by large blocks of colluvium, and in one experiment there is a direct fault displacement that results in a fault scarp overhang. The models with backthrusts have a short fault seed length (25% total sediment thickness) and, thus, more unruptured sediment above the fault tip (3.75 m) to reach the surface. This localizes the deformation to a triangular wedge above the fault, as the fault initially steepens to reach the surface (Fig. 10d; see Figs. S2 and S3). The three experiments with a colluvial wedge are dominated by large, cohesive blocks of colluvium that collapse into the toe of the fault scarp after sufficient vertical motion on the fault at depth. Finally, the one experiment representing a direct fault displacement occurs in a trial of sufficiently strong, cohesive sediment (2.0 MPa) to resist hanging-wall collapse. The experiment represents a case with only 1.25 m of unruptured sediment above the fault tip. Thus, the new rupture on this

**Figure 9.** The contact bonds are depicted for 15 models on a 20°, 40°, and 60° dipping fault across a range of sediment strength mechanics based on the cohesion and tensile strengths of the contact bonds (0.1, 0.5, 1.0, 1.5, and 2.0 MPa). These experiments correspond to a fault seed 50% of the total sediment thickness (5.0 m), indicating that there is 2.5 m of unruptured sediment above the fault tip prior to slip. The red corresponds to bonded particles, and blue corresponds to broken bonds. Table S3 reports the parameters used in these models. The experiment in Figure 7 is the 0.5 MPa sediment on a 40° fault dip, and the experiments from Figure 8 are the middle row (1.0 MPa sediment) after 5.0 m of accumulated slip.

fault utilizes the preserved fault plane from the previous ruptures. Across the wide range of morphologies observed in the strong sediment on a  $40^{\circ}$  dipping fault, these experiments have the maximum deformation zone width of  $\sim$ 8.5 m and an average scarp dip of 28.5° (Fig 10d).

The steep fault (60°) experiments in weak sediment have a wide zone of deformation (~13.4 m) formed through a triangular wedge of distributed shear and have a fault scarp dip of 19.1° (Fig. 10e). However, the strong sediment on a steep fault (60°) experiments have more variation in the resultant ground surface morphology (Fig. 10f). Four of the steep fault (60°) experiments in strong sediment (Fig. 10f) depict a direct fault displacement that is representative of the fault orientation at depth due to the brittle, cohesive strength of the sediment with a small pile of colluvium at the base. These experiments have the smallest deformation zone width (~2.0 m) representative of the motion on the fault at depth. One experiment in 1.5 MPa sediment has large blocks of colluvium that collapsed from a tensile fracture at the crest of the scarp into a wedge with the widest deformation zone (~6.8 m). Finally, the last experiment shows a shallow fault scarp overhang (~34°) that

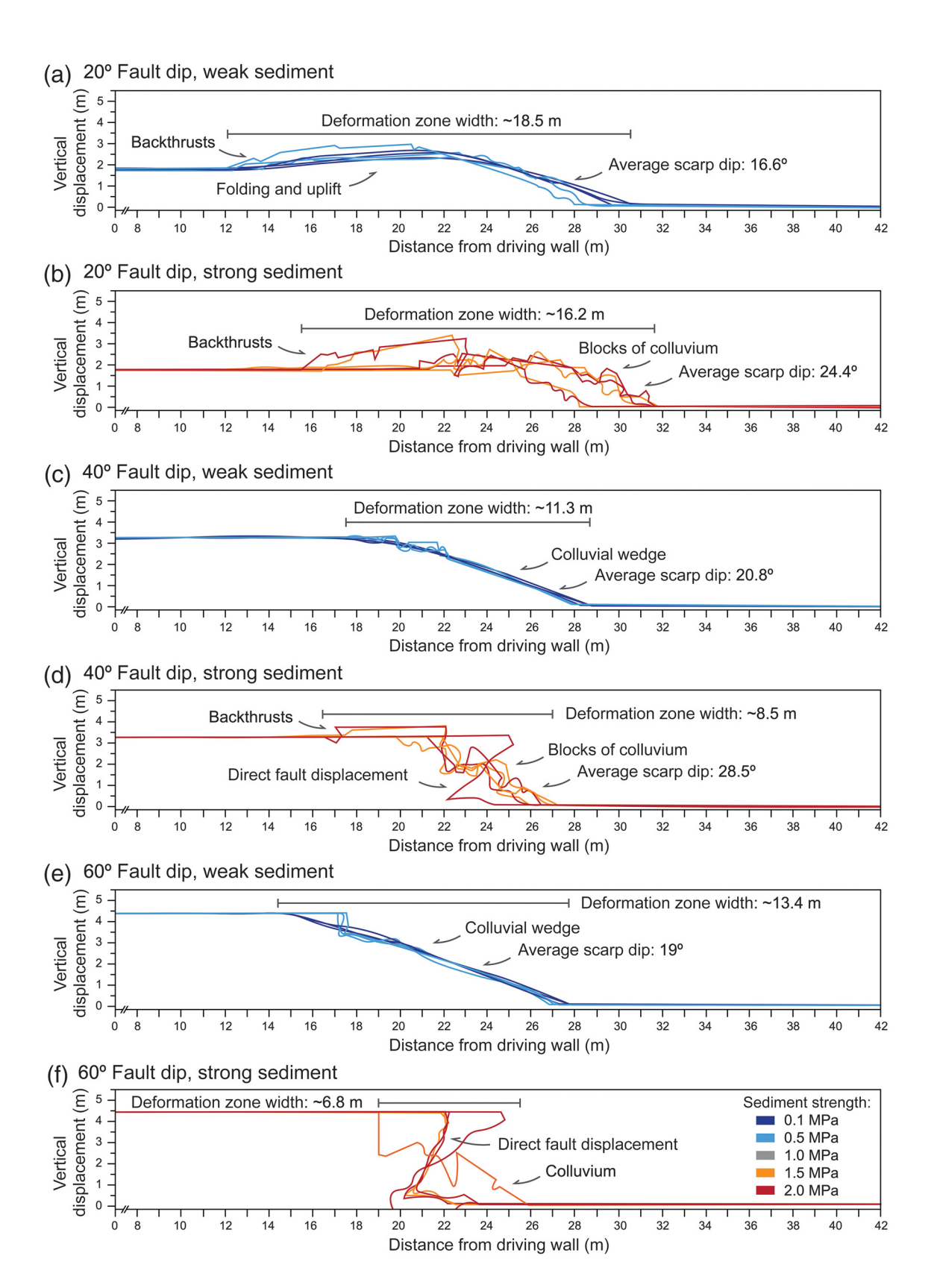


**Figure 10.** Comparison of ground surface deformation profiles across a series of 36 experiments varying fault dip and sediment strength for dense sediment after 5.0 m of accumulated slip, and 1.25, 2.5, and 3.75 m of unruptured sediment above the fault tip. (a) Topographic profiles for six experiments on a fault dip of 20° for weak sediment (0.1–0.5 MPa). (b) Topographic profiles for six experiments on a fault dip of 20° for strong

sediment (1.5–2.0 MPa). (c) Topographic profiles for six experiments on a fault dip of 40° for weak sediment (0.1–0.5 MPa). (d) Topographic profiles for six experiments on a fault dip of 40° for strong sediment (1.5–2.0 MPa). (e) Topographic profiles for six experiments on a fault dip of 60° for weak sediment (0.1–0.5 MPa). (f) Topographic profiles for six experiments on a fault dip of 60° for strong sediment (1.5–2.0 MPa).

does not represent the orientation of the fault at depth (60°) but rather represents a fracture that formed near the friction angle (32°) of the sediment at the onset of deformation (Fig. 10f). The sediment is sufficiently strong to resist hanging-wall collapse, and the fault scarp subsequently maintained this shallow overhang with increasing vertical displacement on the fault at depth (Fig 10f).

# **DISCUSSION**

We categorize the surface ruptures present in our 45 experiments into three groups based on scarp morphology. These groups include: (1) monoclinal scarps; (2) pressure ridges; and (3) simple scarps (Fig. 11a,c,e), with our naming of these groups based on integration and refinement of the terminology proposed by Philip *et al.* (1992) and Rimando *et al.* (2019). Each type of fault scarp morphology can be modified by hanging-wall collapse (Fig. 11b,d,f). Figure 11 presents each of the scarp type morphologies with a representative DEM model example, a natural example of the scarp morphology, and a plot of all the DEM surface profiles that fit that scarp type morphology out of the total 45 experiments performed.

# Monoclinal scarps

Monoclinal scarps generally form in weak sediment on a steep (>30°) fault with representative experiments plotted in Figure 11a. In this class, the fault propagates up through the sediment and forms a triangular wedge of sheared sediments, similar to the mechanism of trishear fault propagation folding (Ersley, 1991; Allmendinger, 1998; Hardy and Finch, 2007; Hughes and Shaw, 2015). In cases in which the fault reaches the surface as a discrete feature, the scarp can be further amplified by displacement of strata above the fault tip by fault-bend folding (Suppe, 1983). The fault scarp consists of a single monoclinal dip panel that typically increases its width and dip (limited by the angle of repose, ~20°) as a function of fault displacement. We adopt the term "monoclinal" to refer to the scarp morphology as a single dip panel based on Rimando et al. (2019). In experiments in which the sediment is weak, the scarp tends to settle during growth by developing a colluvial wedge of sediment that forms above the footwall. In cases in which the sediment is strong, collapse of the scarp is dominated by brittle deformation with blocks detaching and sliding down the face of the scarp. The hanging-wall collapse is accommodated by tensile fractures at the crest of the scarp with distinct blocks of colluvium that rotate into the toe of the wedge. Given that this process is distinct from that which forms the scarp, and produces substantially different patterns of surface deformation, we describe these features as monoclinal collapse scarps (Fig. 11b). In comparison to monoclinal scarps, these monoclinal collapse scarps have a smaller deformation zone width (5.5-9.8 m) because they tend to form in sediments with higher cohesive strengths in which settling is accommodated by tensile fractures and detached blocks that

form during scarp collapse (Fig. 11a,b). As a result, monoclinal collapse scarps tend to have steeper average scarp dips (28.5°).

Monoclinal fault scarps produced in our experiments are similar to local rupture patterns observed in many large earthquakes around the world. The 2008 M 7.9 Wenchuan earthquake locally produced monoclinal fault scarps along the Pengguan fault, which shallowly dips ~20°-30° to the northwest that had a smooth topographic profile without evidence of distributed fracturing at the surface (Fig. 11a; Xu et al., 2009; Fu et al., 2011). Examples of monoclinal collapse scarps formed in the 1988 M 6.9 Armenian earthquake, which ruptured a series of segments along the Spitak fault (Philip et al., 1992). As illustrated in Figure 11b from the central branch of the Spitak fault, tensile fractures form at the crest of the fault scarp with blocks of sediment that collapsed in mass wasting similar to the DEM experiments with strong sediments (Institute of Geological Sciences, Republic of Armenia, photo by Karakhanyan, 1988; Philip et al., 1992). Furthermore, there is considerable along-strike variability in the field rupture from the Armenian earthquake, which is due to the distribution of cohesive blocks of colluvium (Fig. 11b; Institute of Geological Sciences, Republic of Armenia, photo by Karakhanyan, 1988).

# Pressure ridge scarps

Pressure ridge scarps generally form in weak sediment on shallow faults (≤40°), and are a distinctive morphology due to the folding and uplift which extend over the width of the deformation zone beyond the crest of the fault scarp (Fig. 11c). Compared with monoclinal scarps, our models of pressure ridge scarps tend to have a similar maximum fault scarp dip (19.0°) but with a wider deformation zone (16.2-18.5 m) that features a central region of uplift. Pressure ridge scarps that develop in strong sediment tend to have backthrusts that bound the uplifted zone and feature distributed secondary fractures. In some cases, these features enable settling of the scarp, forming pressure ridge collapse scarps (Fig. 11d). Similar to the monoclinal collapse scarps, the pressure ridge collapse scarps may feature distinct blocks of colluvium that collapse into the toe of the fault scarp and steepen the average fault scarp angle (26°). Both the types of pressure ridge scarps (Fig. 11c,d) are defined by a wide zone of distributed deformation with a component of vertical uplift due to folding and fracturing.

Pressure ridge scarps, including backthrusts, were observed locally in the 1999 M 7.6 Chi-Chi and 2008 M 7.9 Wenchuan ruptures (Chen *et al.*, 2001, 2007; Xu *et al.*, 2009; Li *et al.*, 2010; Yu *et al.*, 2010), and were widespread in the 1988 M 6.9 Armenian earthquake (Philip *et al.*, 1992; see Fig. 2e). Many of these natural examples show evidence of hanging-wall collapse and thus are best described as pressure ridge collapse scarps. Similar to our models that produced this class of scarp, these earthquake ruptures generally occurred on moderately

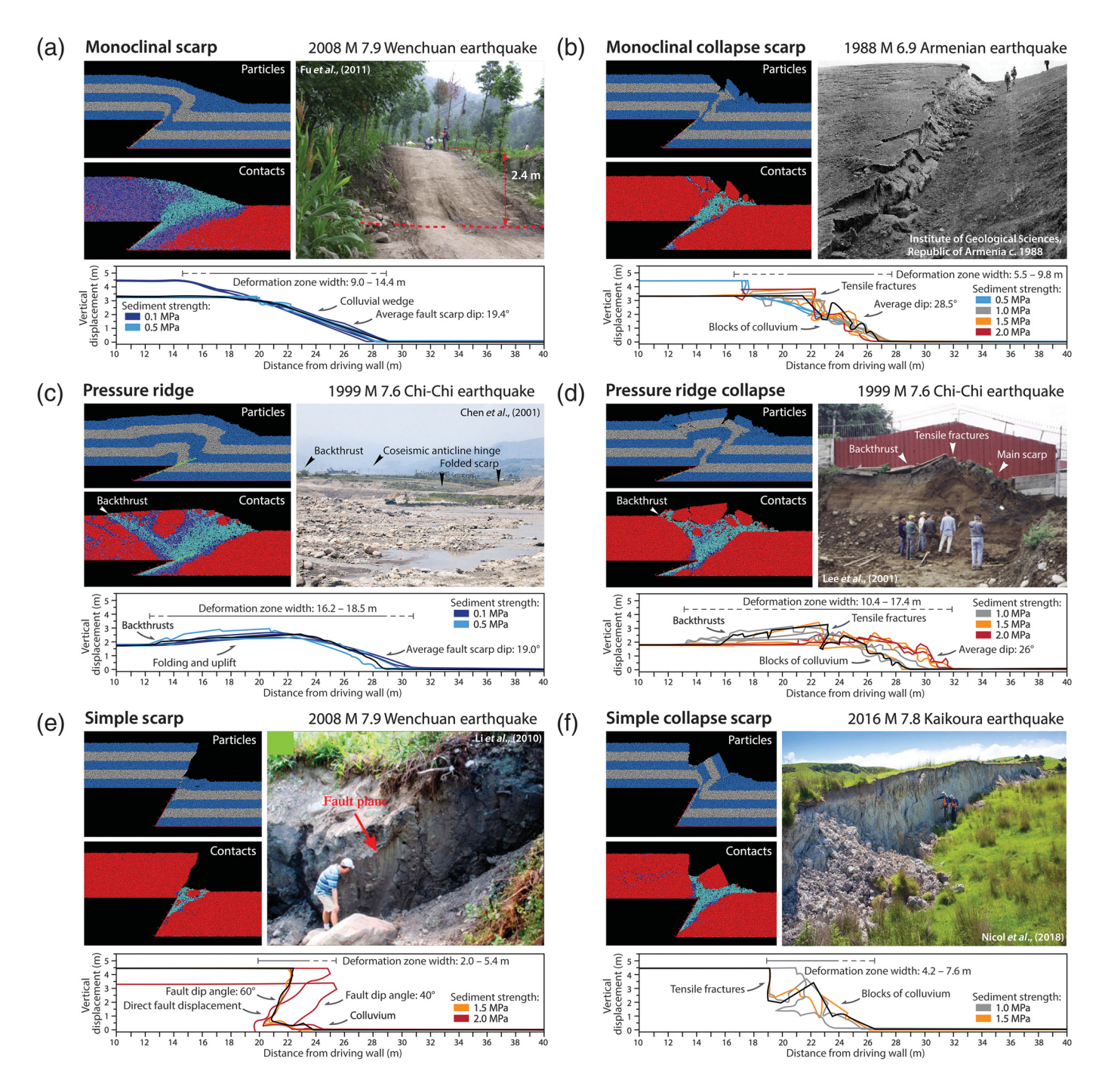


**Figure 11.** Proposed classification system for fault scarp types: (a,b) monoclinal scarp; (c,d) pressure ridge; and (e,f) simple scarp with a representative DEM model of the scarp morphology. Plots show fault scarp profiles from the 45 DEM experiments organized by scarp type and colored by sediment strength mechanics (0.1 MPa indicated in dark blue; 0.5 MPa indicated in light blue; 1.0 MPa indicated in gray; 1.5 MPa indicated in orange; and 2.0 MPa indicated in dark red). The representative example DEM model profiles are identified as black lines in the plots. (a) DEM model with sediment strength of 0.1 MPa on a fault dipping 40°. Field photo from the 2008 Wenchuan, China, earthquake (reprinted with permission from Fu *et al.*, 2011). Plot shows nine DEM topographic profiles. (c) DEM model with sediment strength of 0.5 MPa on a fault dipping 20°. Field photo from the 1999 Chi-Chi, Taiwan, earthquake (reproduced from Chen *et al.*, 2001). Plot shows six DEM topographic profiles. (e) DEM model with sediment strength of 2.0 MPa on a fault dipping 60°. Field

photo from the 2008 Wenchuan, China, earthquake depicting the fault plane and striations (reprinted with permission from Li *et al.*, 2010). Plot shows six DEM topographic profiles. (b) DEM model with sediment strength of 2.0 MPa on a fault dipping 40°. Field photo from the 1988 Armenian earthquake courtesy of Arkady Karakhanyan (reproduced from the Institute of Geological Sciences, Republic of Armenia, photo by Karakhanyan, 1988). Plot shows 11 DEM topographic profiles. (d) DEM model with sediment strength of 2.0 MPa on a fault dipping 20°. Field photo from the 1999 Chi-Chi, Taiwan, earthquake (reproduced from Lee *et al.*, 2001). Plot shows nine DEM topographic profiles. (f) DEM model with sediment strength of 1.0 MPa on a fault dipping 60°, and field photo from the 2016 Kaikoura earthquake in New Zealand with alongstrike variation in the fault rupture (photography by Kate Pedley, reproduced from Nicol *et al.*, 2018). Plot shows four DEM topographic profiles. Matrices of the full DEM model results are included in Figures S2 and S3.

dipping fault planes (Philip et al., 1992; Chen et al., 2001, 2007; Xu et al., 2009; Li et al., 2010; Yu et al., 2010).

# Simple fault scarps

Simple fault scarps represent cases in which sufficiently cohesive sediments or soils yield a fault scarp overhang due to displacement on a fault at depth (Fig. 11e). These scarps form more commonly in our models with steep faults (>30°). These simple scarps have the smallest deformation zone width (2.0–5.4 m) of the three classes. The hanging walls of simple scarps often collapse, generating large, cohesive blocks of colluvium that extend the deformation zone width (4.2–7.6 m). We refer to these as simple collapse scarps (Fig. 11f).

Simple fault scarps were observed locally in the 2008 M 7.9 Wenchuan (Fig. 11e), 2013 M 7.2 Bohol, Philippines, and 2016 M 7.8 Kaikoura (Fig. 11f) ruptures (Li et al., 2010; Nicol et al., 2018; Rimando et al., 2019). In these cases, the simple thrust scarp morphology directly represents the fault dip because the cohesion of the sediment is sufficiently strong to resist collapse of the hanging wall (Rimando et al., 2019). Many, if not most, simple scarps experience hanging-wall collapses. Such a simple scarp was observed in the 2008 Wenchuan earthquake with direct fault displacements and striations preserved on an exposed section of the Beichuan fault, dipping 75°-80° to the northwest (Fig. 11e; Li et al., 2010). In addition, the 2016 Kaikoura rupture locally represents a simple scarp with lateral variation in morphology to form simple collapse scarps (Fig. 11f; Nicol et al., 2018). The field photo in Figure 11f of the Kaikoura rupture occurs along the north-south-trending portion of the leader fault (dipping ~ 70° ± 10° W), which experienced leftlateral reverse motion. At this location of the field photo, displacement was primarily reverse (3.5 ± 0.5 m), resulting in a simple scarp with striations preserved on the lower 2.0 m of the scarp (Nicol et al., 2018). Indeed, simple scarps are difficult to preserve in nature and are relatively uncommon (Rimando et al., 2019). We suggest that our DEM models can capture this variability by effectively replicating the range of possible sediment mechanics for a given fault of a specified amount of accumulated slip and dip.

Overall, our models show variability in the style of deformation across all scarp types based on sediment strength. Furthermore, sediment strength can determine which type of scarp forms at a given amount of fault displacement. Weak sediment (Fig. 11, 0.1 MPa, indicated in blue) undergoes ductile, distributed deformation and folding, and, thus, tends to lead to monoclinal or pressure ridge scarps. In contrast, strong sediment (Fig. 11, 2.0 MPa, indicated in red) is dominated by brittle, localized deformation, and commonly leads to pressure ridge collapse or simple scarps. Our outcomes closely resemble the results of Hughes (2020) in which high values of cohesion led to brittle faulting and localized shear, whereas low values of cohesion led to wider zones of distributed deformation in 2D DEM fold-and-thrust belt models. Weak sediment

models have gently dipping surface scarps limited in slope by the angle of repose (~20°). Strong sediment features variable patterns of surface deformation controlled by the formation of fault scarps that directly reflect the orientation of the fault plane, associated tensile fracturing, and slumping. Thus, the pattern of surface deformation at different fault dips is variable and closely related to the strength of the sediment. By incorporating such variations in our DEM models, they effectively reproduce a wide range of observed behaviors in natural fault scarps (Philip *et al.*, 1992; Fu *et al.*, 2011; Nicol *et al.*, 2018; Rimando *et al.*, 2019).

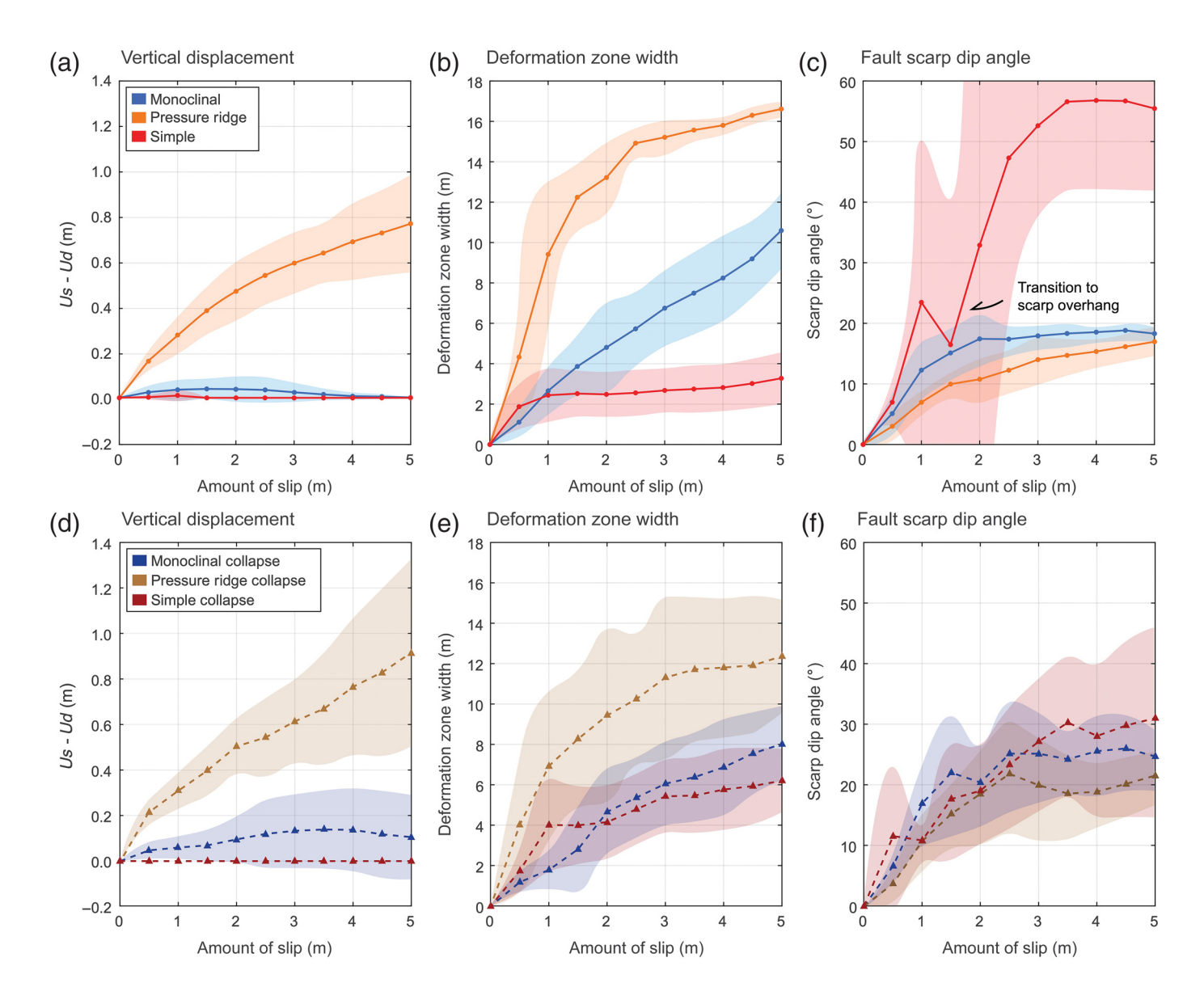
# **EVALUATION OF SURFACE DEFORMATION CHARACTERISTICS**

Our suite of models effectively reproduces a range of natural ground rupture styles for thrust and reverse-fault earthquakes (Fig. 11). This motivated us to evaluate these models systematically to define key parameters that influence observed surface deformation patterns and better understand how specific characteristics of surface deformation that impact hazard (vertical uplift, width of deformation zone, and fault scarp dip) relate to fault displacement and, in turn, earthquake magnitudes.

We measured the maximum vertical displacement, deformation zone width, and fault scarp dip for each of the 45 experiments represented in Figure 11. We show the average  $\pm 2\sigma$  (standard deviation) of these values for each of the scarp classifications in Figure 12 as a function of the amount of accumulated slip on a fault at depth. Notably, the range of scarp characteristics defined by these  $\pm 2\sigma$  values show that the three classes of scarps are generally distinct from one another after  $\sim 1.5$  m of slip (Fig. 12a–c). Furthermore, this representation allows us to define how scarp characteristics evolve with increasing slip (i.e., earthquake magnitude) and offers insight into the key model parameters (e.g., fault dip and sediment strength) that influence these relationships.

The primary control on the style of surface deformation in our models is the magnitude of slip on the fault. The maximum fault scarp height, measured as the vertical distance between the highest elevation of the scarp relative to the undeformed surface of the footwall, directly increases with the accumulation of slip on a fault at depth (see Fig. 7). Of the three main classes of fault scarps represented in our experiments, the simple scarps experience the most vertical displacement  $(4.1 \pm 0.5 \text{ m})$ , followed by monoclinal scarps  $(3.4 \pm 0.6 \text{ m})$ , and finally pressure ridge scarps  $(2.5 \pm 0.2 \text{ m})$  with the total accumulation of slip at depth of 5.0 m across all experiments (Fig. 12a). The variation in the relationship between vertical displacement and slip reflects the fault dip at depth, as simple scarps tend to form on steep faults  $(60^{\circ})$ , monoclinal scarps often form on a moderately dipping fault  $(40^{\circ})$ , and pressure ridges typically occur on shallow faults  $(20^{\circ})$ .

In Figure 12a,d, we show the measured maximum scarp height (Us) minus the vertical displacement associated with fault slip at depth (Ud). The vertical displacement of the hanging wall



at the base of the model corresponds to the observed displacement of the scarp at the surface. As expected, the monoclinal, simple, and their associated collapse scarps have vertical uplift at the surface that generally equals the vertical uplift at depth. As a result, the curves for monoclinal and simple scarps are approximately equal to zero in Figure 12a,d. Notably, the pressure ridge and their associated collapse scarps accumulate additional uplift beyond the amount imposed by the fault at depth. Thus, pressure ridge and their associated collapse scarps have more uplift at the surface than along the fault at depth—positive values of the maximum scarp height (*Us*) minus the vertical displacement at depth (*Ud*) (Fig. 12a,d). This behavior is due to the significant folding and secondary faulting (including backthrusts) that are common in pressure ridge scarps.

The width of the deformation zone and fault scarp dip also increase with accumulation of slip on the fault for each class of scarp (Fig. 12b,e). Monoclinal scarps, which result from moderate to high-fault dips (40° and 60°) in weak sediments, generally localize deformation to a triangular wedge above the

Figure 12. Measurements of the average surface deformation characteristics over the accumulation of slip on a fault for the experiments presented in Figure 11. The 45 experiments are organized by the proposed fault scarp classification (monoclinal scarps indicated in blue, monoclinal collapse scarps indicated in dark blue, pressure ridge scarps indicated in orange, pressure ridge collapse scarps indicated in brown, simple scarps indicated in bright red, and simple collapse scarps indicated in dark red), and the average  $\pm 2\sigma$  values of the maximum vertical displacement, deformation zone width, and fault scarp dip are plotted on the y axis. (a) The maximum fault scarp height (Us: relative to the undeformed surface of the footwall block) minus the vertical displacement on the fault at depth (Ud) is plotted as a function of slip for each class of scarp. (b) The maximum deformation zone width of the fault scarps is plotted as a function of slip for each class of scarp. (c) The average fault scarp dip is plotted as a function of slip for each class of scarp. (d,e,f) Similar plots for monoclinal collapse, pressure ridge collapse, and simple collapse scarps. Note that in panel (d), the  $\pm 2\sigma$  band is not present for simple collapse scarps. This is because there is no variation in the measurements of vertical displacement between these experiments. There is a direct relationship with the vertical displacement of the hanging wall at depth to the observed displacement of the scarp at the surface for simple collapse scarps. The DEM model parameters and scarp characteristics measurements are included in the supplemental material.

fault tip. These models do not have a tendency to develop secondary faults, including backthrusts, at large distances from the main rupture. Thus, deformation zone width tends to increase linearly with fault slip (Fig. 12b; see Figs. 7 and 11). In contrast, pressure ridge scarps, which tend to result from models with a low-fault dip (20°), generally exhibit a wider zone of deformation compared to monoclinal scarps at low amounts of fault slip. This reflects the development of backthrusts at low amounts of fault slip that, combined with the forethrusts, define the width of the deformation zone (Fig. 12b). The triangular zone of deformation between the backthrusts and forethrusts is influenced by the amount of unruptured sediment above the fault tip. Experiments with a thicker section of unruptured sediments tend to have a wider zone of deformation compared to experiments with a thinner section of unruptured sediments. This relationship is clearer for strong sediment (>1.0 MPa), whereas weak sediment experiments are dominated by contact bond breakage and particle rolling. Once this deformation zone is established, the widths of pressure ridge scarps tend to increase gradually with increasing slip.

The simple scarps, which tend to form with steeper fault dips and stronger sediment strengths, feature the smallest deformation zone widths. Typically, these scarps start with a distributed zone of shear at low accumulations of slip (<1.5 m) with a morphology of deformation zone width and scarp dip similar to monoclinal scarps. However, once the simple scarp is established (>1.5 m of accumulated slip), the width grows at a steady rate with increasing slip. This width directly reflects the horizontal overlap of the hanging wall and footwall at the imposed fault dip.

The rate of increase in scarp dip varies substantially across the scarp classes, which, in turn, reflects fault dip and sediment strength. In monoclinal scarps, surface dip increases linearly with fault displacement to a value that represents the angle of repose. This behavior reflects that monoclinal scarps generate a triangular wedge of colluvium, which reaches the angle of repose and then undergoes episodes of gravitational collapse to maintain this angle. For monoclinal scarps in weak sediment presented in our models, the angle of repose is  $18.8^{\circ} \pm 1.1^{\circ}$ ; for strong sediment, this value is 26.0° ± 6.2° (Fig. 12c,f). Pressure ridge scarps show a similar pattern because their average dip is generally represented by the slope that forms above the forethrust, which is akin to a monoclinal scarp. Simple scarps generate the steepest surface slopes for a given amount of fault slip because they tend to form in strong sediment (Fig. 12c). However, many models exhibit a transition from small monoclinal scarps at low fault slip to simple scarps at larger amounts of displacement, which can produce a nonlinear relationship between scarp dip and slip.

Collapse of all the three classes of scarps does not change vertical displacement and has a limited influence on scarp width (Fig. 12d,e). The most significant influence of collapse is on scarp dip (Fig. 12f). The collapse process generally involves tensile fractures or normal faults forming at the crest of the fault scarp, similar to the patterns observed in analog sandbox and 3D DEM models in Takao et al. (2014). This process occurs in experiments in which the cohesive and tensile strengths of the sediment are not sufficiently strong to resist hanging-wall collapse. Regarding morphological characteristics, collapse tends to reduce the width of monoclinal and pressure ridge scarps for a given amount of slip; whereas simple scarps tend to increase in width for a given amount of slip due to blocks sliding into the footwall (these features are included as part of scarp width; Fig. 12b,e). Collapse tends to slightly increase the dip of monoclinal and pressure ridge scarps due to the formation of steeply dipping tensile fractures (Fig. 12c,f). However, it significantly reduces the dip of simple scarps (Fig. 12c,f). Thus, collapse tends to reduce the differences in scarp dip for a given amount of slip among the three scarp classes (Fig. 12f).

#### APPLICATION TO HAZARD ASSESSMENT

The ultimate goal of our work is to help better forecast ground surface deformation patterns that will result from future large earthquakes. These results, and the work of others (Takao *et al.*, 2014; Chang *et al.*, 2015; Garcia and Bray, 2018a,b; Hughes, 2020), show that DEM models can effectively reproduce ground rupture characteristics for a range of faulting and sediment parameters. This suggests that DEM models can be used in a deterministic manner to forecast scarp characteristics for a given earthquake scenario. In such applications, fault displacement in the models can be related to earthquake magnitude through widely used empirical relationships (Wells and Coppersmith, 1994), such as the rupture area (Hanks and Bakun, 2002, 2008), average displacement (Biasi and Weldon, 2006), and documented slip rates (Brankman and Shaw, 2009).

Fault displacement hazard analysis aims to forecast a range of ground rupture characteristics, such as fault displacement amplitude, probability of distributed faulting, fault zone width, and location uncertainty (Youngs et al., 2003; Moss and Ross, 2011; Petersen et al., 2011; Boncio et al., 2018). Fault displacement models currently rely on statistical analysis of empirical data from historical surface-rupturing earthquakes (Baize et al., 2020; Sarmiento et al., 2021); although progress in dynamic rupture simulations from depth to the ground surface has been progressing (Wang and Goulet, 2021). Because the number of sufficiently documented earthquakes is limited, there are gaps in the statistics that result in epistemic uncertainty in the FDHA models. For reverse and reverse-oblique faults, current research efforts only have 25 sufficiently documented events to populate surface fault rupture measurements needed to develop FDHA models (Sarmiento et al., 2021). Our DEM research augments field measurements by exploring: fault dips not well represented in the empirical database, material properties and their influence on the maximum displacement and the surface displacement field, fault scarp classification and observed trends in field measurements, and suites of fault rupture events to further populate the sample space. Thus, we suggest that DEM models of fault surface rupture, along with other numerical modeling efforts, can help supplement natural datasets used to develop fault displacement models.

# **CONCLUSIONS**

We present a series of DEM models of fault scarp formation that are calibrated against analog and numerical models to investigate factors that influence the variability of scarp geometries observed in large earthquakes. Our results indicate that the magnitude of fault slip, fault dip, and sediment strengths have important controls on the styles and patterns of ground surface deformation. The fault scarp dip and deformation zone width increase with slip on the fault. Fault dip also exhibits a major control on the resultant internal and surface deformation. Lower fault dips result in a broad zone of surface deformation with distributed folding, faulting, and secondary fractures, whereas higher fault dips result in deformation localized to the primary fault scarp above the fault tip. Finally, weak sediment mechanics lead to distributed deformation, whereas strong sediment mechanics lead to localized shear planes and brittle deformation with sharp, steeply dipping fault scarps.

We developed a series of fault scarp morphology classifications based on a range of models with variable sediment strength mechanics and fault dips by building on the terminology presented in Philip *et al.* (1992) and Rimando *et al.* (2019). We identified three main classes of fault scarp morphology represented in our experiments:

- 1. Monoclinal scarps: These have a smooth, single dip panel that increases in width and dip with increasing slip on a fault at depth. These scarps commonly form in weak sediment above steep (>30°) faults.
- Pressure ridges: These represent cases in which folding and/ or backthrusts define a wide zone of deformation that is generally maintained as fault slip increases. These scarps commonly form in weak sediment on shallow faults (<30°).</li>
- 3. Simple scarps: These have direct fault displacements that represent the dip of the fault at depth and resist collapse from the cohesive strength of the material. They commonly form in strong sediment above steep faults (>30°).

Each of these classifications has a related case that is modified by tensile fracturing and subsequent hanging-wall collapse. Relationships suggested by our models between fault displacement and key surface deformation features (vertical displacement, scarp width, and scarp dip) provide insights that can help forecast ground rupture patterns for a range of earthquake magnitudes, fault geometries, and sediment strengths.

# **DATA AND RESOURCES**

The Particle Flow Code 2D (PFC2D v.7.00) projects and associated files for the Cole and Lade (1984), Bransby *et al.*, (2008), and Garcia and Bray (2018a) replica models as well as a 2D distinct element method (DEM) model code (used for Figs. 7–11) and the code framework for a general biaxial stress test are available at <a href="https://github.com/kchiama?tab=repositories">https://github.com/kchiama?tab=repositories</a> (last accessed April 2023) for reproducibility. The supplemental material contain detailed methods for the generation of a DEM model and descriptions of the microproperties. Furthermore, the supplemental material defines the parameters for the models presented in this article and images of the 45 model results shown in Figures 11 and 12. A dataset of the 45 DEM experiments with associated parameters and measured surface deformation characteristics is included in the supplemental material.

# **DECLARATION OF COMPETING INTERESTS**

The authors acknowledge that there are no conflicts of interest recorded.

### **ACKNOWLEDGMENTS**

This work was supported using Aspen Emerson Paradigm SKUA-GOCAD, as well as Itasca, Particle Flow Code 2D (PFC2D) version 6.00 and 7.00. The authors would specifically like to thank the Itasca support and developers for their guidance in developing the model structure and code. This research was supported by the National Science Foundation (NSF), Division of Earth Sciences (EAR), Tectonics Program, Grant Number 2207119; and by the Southern California Earthquake Center (SCEC) Agreement Number 110862181 (SCEC Award Number 22013), which is funded by the prime award National Science Foundation Award Number EAR-1600087. The authors thank Fernando E. Garcia for thoughtful discussion and guidance on replicating his 3D distinct element method (DEM) models. The authors also thank Jessica Don, Michael Naylor Hudgins, Brendan Meade, Natasha Toghramadjian, Robert Welch, and Franklin Wolfe for thoughtful discussions and coding suggestions. The authors thank the reviewers for their comments and suggestions that greatly improved the article.

#### **REFERENCES**

Allmendinger, R. W. (1998). Inverse and forward numerical modeling of trishear fault-propagation folds, *Tectonics* **17**, no. 4, 640–656, doi: 10.1029/98TC01907.

Baize, S., F. Nurminen, A. Sarmiento, T. Dawson, M. Takao, O. Scotti, T. Azuma, P. Boncio, J. Champenois, F. R. Cinti, et al. (2020). A worldwide and unified database of surface ruptures (SURE) for fault displacement hazard analyses, Seismol. Res. Lett. 91, no. 1, 499–520, doi: 10.1785/0220190144.

Bayer, K. (2017). Mixed emotions in Kaikoura ahead of massive magnitude-7.8 earthquake's one-year anniversary, *New Zealand Herald*, available at https://www.nzherald.co.nz/nz/mixed-emotions-in-kaikoura-ahead-of-massive-magnitude-78-quakes-one-year-anniversary/INRZHEHBOMLQBM7GTJUFGWP7CY/ (last accessed April 2023).

Benesh, N. P., A. Plesch, J. H. Shaw, and E. K. Frost (2007). Investigation of growth fault bend folding using discrete element modeling: Implications for signatures of active folding above blind

- thrust faults, *J. Geophys. Res.* **112**, no. 3, 1–10, doi: 10.1029/2006[B004466.
- Biasi, G. P., and R. J. Weldon (2006). Estimating surface rupture length and magnitude of paleoearthquakes from point measurements of rupture displacement, *Bull. Seismol. Soc. Am.* **96,** no. 5, 1612–1623.
- Boncio, P., F. Liberi, M. Caldarella, and F. C. Nurminen (2018). Width of surface rupture zone for thrust earthquakes: Implications for earthquake fault zoning, *Nat. Hazards Earth Syst. Sci.* **18**, no. 1, 241–256, doi: 10.5194/nhess-18-241-2018.
- Brankman, C. M., and J. H. Shaw (2009). Structural geometry and slip of the Palos Verdes fault, southern California: Implications for earthquake hazards, *Bull. Seismol. Soc. Am.* **99**, no. 3, 1730–1745.
- Bransby, M. F., M. C. R. Davies, A. El Nahas, and S. Nagaoka (2008). Centrifuge modelling of reverse fault-foundation interaction, *Bull. Earthq. Eng.* **6**, no. 4, 607–628, doi: 10.1007/s10518-008-9080-7.
- Bray, J. D., J. D. Frost, E. M. Rathje, and F. E. Garcia (2019). Recent advances in geotechnical post-earthquake reconnaissance, *Front. Built Environ.* **5**, doi: 10.3389/fbuil.2019.00005.
- Chang, Y. Y., C. J. Lee, W. C. Huang, W. Y. Hung, W. J. Huang, M. L. Lin, and Y. H. Chen (2015). Evolution of the surface deformation profile and subsurface distortion zone during reverse faulting through overburden sand, *Eng. Geol.* 184, 52–70, doi: 10.1016/j.enggeo.2014.10.023.
- Chen, W. S., B. S. Huang, Y. G. Chen, Y. H. Lee, C. N. Yang, C. H. Lo, H. C. Chang, Q. C. Sung, N. W. Huang, C. C. Lin, et al. (2001). 1999 Chi-Chi earthquake: A case study on the role of thrust-ramp structures for generating earthquakes, Bull. Seismol. Soc. Am. 91, no. 5, 986–994, doi: 10.1785/0120000731.
- Chen, W. S., C. C. Yang, I. C. Yen, L. S. Lee, K. J. Lee, H. C. Yang, H. C. Chang, Y. Ota, C. W. Lin, W. H. Lin, and T. S. Shih (2007). Late Holocene paleoseismicity of the southern part of the Chelungpu fault in central Taiwan: Evidence from the Chushan excavation site, *Bull. Seismol. Soc. Am.* 97, no. 1, 1–13, doi: 10.1785/0120050161.
- Cluff, L. S., R. A. Page, D. B. Slemmons, and C. B. Crouse (2003).
  Seismic hazard exposure for the Trans-Alaska pipeline, Sixth U.S. Conf. and Workshop on Lifeline Earthquake Engineering, ASCE Technical Council on Lifeline Earthquake Engineering, 10–13 August 2003, Long Beach, California, 535–546.
- Cole, D. A., and P. V. Lade (1984). Influence zones in alluvium over dip-slip faults, *J. Geotech. Eng.* **110**, no. 5, 599–615, doi: 10.1061/ (ASCE)0733-9410(1984)110:5(599).
- Cundall, P. A., and O. D. L. Strack (1979). A discrete numerical model for granular assemblies, *Geotechnique* **29**, no. 1, 47–65.
- Erickson, S. G., L. M. Strayer, and J. Suppe (2001). Initiation and reactivation of faults during movement over a thrust-fault ramp: Numerical mechanical models, *J. Struct. Geol.* **23**, no. 1, 11–23, doi: 10.1016/S0191-8141(00)00074-2.
- Erickson, S. G., L. M. Strayer, and J. Suppe (2004). Numerical modeling of hinge-zone migration in fault-bend folds, chapter 22, in *Thrust Tectonics and Hydrocarbon Systems*, K. R. McClay (Editor), Vol. 82, AAPG Memoir, Tulsa, Oklahoma, 438–452, doi: 10.1306/M82813C23.
- Erslev, E. A. (1991). Trishear fault-propagation folding, *Geology* 19, 617–620.
- Finch, E., S. Hardy, and R. Gawthorpe (2003). Discrete element modelling of contractional fault- propagation folding above rigid

- basement fault blocks, *J. Struct. Geol.* **25,** no. 4, 515–528, doi: 10.1016/S0191-8141(02)00053-6.
- Finch, E., S. Hardy, and R. Gawthorpe (2004). Discrete-element modelling of extensional fault-propagation folding above rigid basement fault blocks, *Basin Res.* **16**, 467–488, doi: 10.1111/j.1365-2117.2004.00241.x.
- Fu, B., P. Shi, H. Guo, S. Okuyama, Y. Ninomiya, and S. Wright (2011). Surface Deformation related to the 2008 Wenchuan earthquake, and mountain building of the Longmen Shan, eastern Tibetan plateau, *J. Asian Earth Sci.* **40**, no. 4, 805–824, doi: 10.1016/j.jseaes.2010.11.011.
- Garcia, F. E., and J. D. Bray (2018a). Distinct element simulations of earthquake fault rupture through materials of varying density, *Soils Found.* **58**, no. 4, 986–1000, doi: 10.1016/j.sandf.2018.05.009.
- Garcia, F. E., and J. D. Bray (2018b). Distinct element simulations of shear rupture in dilatant granular media, *Int. J. Geomech.* **18**, no. 9, doi: 10.1061/(asce)gm.1943-5622.0001238.
- Garcia, F. E., and J. D. Bray (2019a). Distinct element analysis of earthquake surface fault rupture through layered media, Earthquake Geotechnical Engineering for Protection and Development of Environment and Constructions—Proc. of the 7th International Conf. on Earthquake Geotechnical Engineering, 17–20 June 2019, Rome, Italy, 2542–2549.
- Garcia, F. E., and J. D. Bray (2019b). Modeling the shear response of granular materials with discrete element assemblages of sphereclusters, *Comput. Geotech.* 106, 99–107, doi: 10.1016/j.compgeo.2018.10.003.
- Guo, Y., and J. K. Morgan (2004). Influence of normal stress and grain shape on granular friction: Results of discrete element simulations, *J. Geophys. Res.* **109**, no. 12, 1–16, doi: 10.1029/2004JB003044.
- Hanks, T. C., and W. H. Bakun (2002). A bilinear source-scaling model for M—log A observations of continental earthquakes, *Bull. Seismol. Soc. Am.* 92, 1841–1846.
- Hanks, T. C., and W. H. Bakun (2008). M-logA observations for recent large earthquakes, *Bull. Seismol. Soc. Am.* 98, no. 1, 490–494.
- Hardy, S., and N. Cardozo (2021). Discrete element modelling of sedimentation and tectonics: Implications for the growth of thrust faults and thrust wedges in space and time, and the interpretation of syn-tectonic (growth) strata, *Front. Earth Sci.* 9, doi: 10.3389/ feart.2021.742204.
- Hardy, S., and E. Finch (2005). Discrete-element modelling of detachment folding, *Basin Res.* **17**, no. 4, 507–520, doi: 10.1111/j.1365-2117.2005.00280.x.
- Hardy, S., and E. Finch (2006). Discrete element modelling of the influence of cover strength on basement-involved fault-propagation folding, *Tectonophysics* **415**, nos. 1/4, 225–238, doi: 10.1016/j.tecto.2006.01.002.
- Hardy, S., and E. Finch (2007). Mechanical stratigraphy and the transition from trishear to kink-band fault-propagation fold forms above blind basement thrust faults: A discrete-element study, *Mar. Pet. Geol.* **24**, no. 2, 75–90, doi: 10.1016/j.marpetgeo.2006.09.001.
- Hubbard, J., and J. H. Shaw (2009). Uplift of the Longmen Shan and Tibetan plateau, and the 2008 Wenchuan (M = 7.9) earthquake, *Nature* **458**, no. 7235, 194–197, doi: 10.1038/nature07837.
- Hughes, A. N. (2020). Mechanical controls on structural styles in short-ening environments: A discrete-element modelling approach, *Geol. Soc. Spec. Publ.* 490, no. 1, 33–55, doi: 10.1144/SP490-2019-114.

- Hughes, A. N., and J. H. Shaw (2015). Insights into the mechanics of fault-propagation folding styles, *Bull. Seismol. Soc. Am.* **127**, nos. 11/12, 1752–1765, doi: 10.1130/B31215.1.
- Hughes, A. N., N. P. Benesh, and J. H. Shaw (2014). Factors that control the development of fault-bend versus fault-propagation folds: Insights from mechanical models based on the discrete element method (DEM), *J. Struct. Geol.* 68, 121–141, doi: 10.1016/j.jsg.2014.09.009.
- Imber, J., G. W. Tuckwell, C. Childs, J. J. Walsh, T. Manzocchi, A. E. Heath, C. G. Bonson, and J. Strand (2004). Three-dimensional distinct element modelling of relay growth and breaching along normal faults, J. Struct. Geol. 26, no. 10, 1897–1911.
- Itasca (1999). PFC2D: Theory and background, User's guide, command reference, FISH in PFC2D, Itasca Consulting Group, Minneapolis, Minnesota, U.S.A.
- Itasca (2021). PFC—Particle flow code, version. 7.0, Itasca, Minneapolis.
  Jaeger, J. C., and N. G. W. Cook (1976). Fundamentals of Rock Mechanics, Second Ed., Chapman and Hall, London, ISBN: 0 412 21410 5.
- Jaeger, J. C., N. G. W. Cook, and R. W. Zimmerman (2007).
  Fundamentals of Rock Mechanics, Second Ed., Blackwell Publishing Ltd., Malden, Massachusetts.
- Kaiser, A., N. Balfour, B. Fry, C. Holden, N. Litchfield, M. Gerstenberger, E. D'anastasio, N. Horspool, G. McVerry, J. J. S. R. Ristau, et al. (2017). The 2016 Kaikōura, New Zealand, earthquake: Preliminary seismological report, Seismol. Res. Lett. 88, no. 3, 727–739, doi: 10.1785/0220170018.
- Karakhanyan, A. (1988) Photograph of Spitak fault rupture from the 1988 Armenian earthquake, Institute of Geological Sciences, Republic of Armenia.
- Kelson, K. I., K. H. Kang, W. D. Page, C. T. Lee, and L. S. Cluff (2001). Representative styles of deformation along the Chelungpu fault from the 1999 Chi-Chi (Taiwan) earthquake: Geomorphic characteristics and responses of man-made structures, *Bull. Seismol. Soc. Am.* 91, no. 5, 930–952, doi: 10.1785/0120000741.
- Kloss, C., C. Goniva, A. Hager, S. Amberger, and S. Pirker (2012). Models, algorithms and validation for opensource DEM and CFD-DEM, *Progr. Comput. Fluid Dynam.* 12, nos. 2/3, 140–152, doi: 10.1504/PCFD.2012.047457.
- Kozicki, J., and F. V. Donzé (2008). A new open-source software developed for numerical simulations using discrete modeling methods, Comput. Methods Appl. Mech. Eng. 197, nos. 49/50, 4429–4443, doi: 10.1016/j.cma.2008.05.023.
- Lade, P. V., D. A. Cole, and D. Cummings (1984). Multiple failure surfaces over dip-slip faults, *J. Geotech. Eng.* 110, no. 5, 616–627, doi: 10.1061/(ASCE)0733-9410(1984)110:5(616).
- Lee, J.-C., Y.-G. Chen, K. Sieh, K. Mueller, W.-S. Chen, H.-T. Chu, Y.-C. Chan, C. Rubin, and R. Yeats (2001). A vertical exposure of the 1999 surface rupture of the Chelungpu fault at Wufeng, western Taiwan: Structural and paleoseismic implications for an active thrust fault, *Bull. Seismol. Soc. Am.* 91, no. 5, 914–929, doi: 10.1785/0120000742.
- Li, Y., D. Jia, J. H. Shaw, J. Hubbard, A. Lin, M. Wang, L. Luo, H. Li, and L. Wu (2010). Structural interpretation of the seismic faults of the Wenchuan earthquake: Three-dimensional modeling of the Longmen Shan fold-and-thrust belt, *J. Geophys. Res.* 115, no. 4, doi: 10.1029/2009JB006824.

- Litchfield, N. J., P. Villamor, R. J. V. Dissen, A. Nicol, P. M. Barnes, A. Barrell, D. J. Pettinga, J. R. Langridge, R. M. Little, T. A. Mountjoy, et al. (2018). Surface rupture of multiple crustal faults in the 2016 Mw 7.8 Kaikōura, New Zealand, earthquake, Bull. Seismol. Soc. Am. 108, no. 3B, 1496–1520, doi: 10.1785/0120170300.
- Mora, P., and D. Place (1998). Numerical simulation of earthquake faults with gouge: toward a comprehensive explanation for the heat flow paradox, *J. Geophys. Res.* **103**, no. B9, doi: 10.1029/98JB01490.
- Mora, P., and D. Place (1999). The weakness of earthquake faults, *Geophys. Res. Lett.* **26**, no. 1, 123–126, doi: 10.1029/1998GL900231.
- Morgan, J. K. (1999). Numerical simulations of granular shear zones using the distinct element method: 2. Effects of particle size distribution and interparticle friction on mechanical behavior, *J. Geophys. Res.* **104**, no. B2, 2721–2732, doi: 10.1029/1998jb900055.
- Morgan, J. K. (2004). Particle dynamics simulations of rate- and state-dependent frictional sliding of granular fault gouge, *Pure Appl. Geophys.* **161**, nos. 9/10, 1877–1891, doi: 10.1007/s00024-004-2537-y.
- Morgan, J. K. (2015). Effects of cohesion on the structural and mechanical evolution of fold and thrust belts and contractional wedges: Discrete element simulations, *J. Geophys. Res.* **120**, 3870–3896, doi: 10.1002/2014JB011455.
- Morgan, J. K., and M. S. Boettcher (1999). Numerical simulations of granular shear zones using the distinct element method: 1. Shear zone kinematics and the micromechanics of localization, *J. Geophys. Res.* **104**, no. B2, 2703–2719, doi: 10.1029/1998JB900056.
- Morgan, J. K., and P. J. McGovern (2005a). Discrete element simulations of gravitational volcanic deformation: 1. Deformation structures and geometries, *J. Geophys. Res.* 110, no. 5, 1–22, doi: 10.1029/2004JB003252.
- Morgan, J. K., and P. J. McGovern (2005b). Discrete element simulations of gravitational volcanic deformation: 2. Mechanical analysis, *J. Geophys. Res.* **110**, no. 5, 1–13, doi: 10.1029/2004JB003253.
- Moss, R. E. S., and Z. E. Ross (2011). Probabilistic fault displacement hazard analysis for reverse faults, *Bull. Seismol. Soc. Am.* **101**, no. 4, 1542–1553, doi: 10.1785/0120100248.
- Moss, R. E. S., M. Buelna, and K. V. Stanton (2018). Physical, analytical, and numerical modeling of reverse-fault displacement through near-surface soils, *Bull. Seismol. Soc. Am.* 108, no. 6, 3149–3159, doi: 10.1785/0120180067.
- Mustoe, G. G. W., J. R. Williams, and G. Hocking (1987). The Discrete Element Method in Geotechnical Engineering, in *Dynamic Behaviour of Foundations and Buried Structures, Developments in Soil Mechanics and Foundation Engineering*, Elsevier, London, United Kingdom, 233–263.
- Naylor, M., H. D. Sinclair, S. Willett, and P. A. Cowie (2005). A discrete element model for orogenesis and accretionary wedge growth, *J. Geophys. Res.* **110**, no. 12, 1–16, doi: 10.1029/2003JB002940.
- Nicol, A., N. Khajavi, J. R. Pettinga, C. Fenton, T. Stahl, S. Bannister, K. Pedley, N. Hyland-Brook, T. Bushell, I. Hamling, et al. (2018). Preliminary geometry, displacement, and kinematics of fault ruptures in the epicentral region of the 2016 Mw 7.8 Kaikoura, New Zealand, earthquake, Bull. Seismol. Soc. Am. 108, no. 3B, 1521–1539, doi: 10.1785/0120170329.
- Nyman, D. J., W. J. Hall, and V. Szymkowiak (2014). Trans-Alaska pipeline seismic engineering legacy, *Tenth U.S. National Conference on Earthquake Engineering*, 21–25 July 2014, Anchorage, Alaska.

- Petersen, M. D., T. E. Dawson, R. Chen, T. Cao, C. J. Wills, D. P. Schwartz, and A. D. Frankel (2011). Fault displacement hazard for strike-slip faults, *Bull. Seismol. Soc. Am.* **101**, no. 2, 805–825, doi: 10.1785/0120100035.
- Philip, H., E. Rogozhin, A. Cisternas, J. C. Bousquet, B. Borisov, and A. Karakhanian (1992). The Armenian earthquake of 1988 December
  7: Faulting and folding, neotectonics and palaeoseismicity, *Geophys. J. Int.* 110, no. 1, 141–158, doi: 10.1111/j.1365-246X.1992.tb00718.x.
- Potyondy, D. O. (2011). Parallel-bond refinements to match macroproperties of hard rock, in D. Sainsbury, R. Hart, C. Detournay, and M. Nelson (Editors), Continuum and Distinct Element Numerical Modeling in Geomechanics 2011 (Proceedings of Second International FLAC/DEM Symposium), Melbourne, Australia, 14–16 February 2011, 459–465, Itasca International, Minneapolis.
- Ran, Y., X. Xu, H. Wang, W. Chen, L. Chen, M. Liang, H. Yang, Y. Li, and H. Liu (2019). Evidence of characteristic earthquakes on thrust faults from paleo-rupture behavior along the Longmenshan fault system, *Tectonics* 38, no. 7, 2401–2410, doi: 10.1029/2019TC005495.
- Rimando, J., M. A. Aurelio, J. D. B. Dianala, K. J. L. Taguibao, K. M. C. Agustin, A. E. G. Berador, and A. A. Vasquez (2019). Coseismic ground rupture of the 15 October 2013 magnitude (Mw) 7.2 Bohol earthquake, Bohol Island, central Philippines, *Tectonics* 38, no. 8, 2558–2580, doi: 10.1029/2019TC005503.
- Sarmiento, A., D. Madugo, Y. Bozorgnia, A. Shen, S. Mazzoni, G. Lavrentiadis, T. Dawson, C. Madugo, A. Kottke, S. Thompson, et al. (2021). Report GIRS 2021-08 fault displacement hazard initiative data base, doi: 10.34948/N36P48.
- Sorensen, S. P., and K. J. Meyer (2003). Effect of the Denali fault rupture on the Trans-Alaska pipeline, Sixth U.S. Conference and Workshop on Lifeline Earthquake Engineering, ASCE Technical Council on Lifeline Earthquake Engineering, Long Beach, California, 10–13 August 2003.
- Stockmeyer, J. M., J. H. Shaw, and S. Guan (2014). Seismic hazards of multisegment thrust-fault ruptures: Insights from the 1906 Mw 7.4-8.2 Manas China, earthquake, Seismol. Res. Lett. 85, no. 4, 801–808, doi: 10.1785/0220140026.
- Strayer, L. M., and P. J. Hudleston (1997). Numerical modeling of fold initiation at thrust ramps, *J. Struct. Geol.* **19**, 551–566, doi: 10.1016/s0191-8141(96)00109-5.
- Strayer, L. M., and J. Suppe (2002). Out-of-plane motion of a thrust sheet during along-strike propagation of a thrust ramp: A distinct-element approach, *J. Struct. Geol.* **24**, no. 4, 637–650, doi: 10.1016/S0191-8141(01)00115-8.
- Strayer, L. M., S. G. Erickson, and J. Suppe (2004). Influence of growth strata on the evolution of fault-related folds—Distinct-element models, *AAPG Mem.* **82**, 413–437.

- Strayer, L. M., P. J. Hudleston, and L. J. Lorig (2001). A numerical model of deformation and fluid-flow in an evolving thrust wedge, *Tectonophysics* **335**, nos. 1/2, 121–145, doi: 10.1016/S0040-1951(01)00052-X.
- Suppe, J. (1983). Geometry and kinematics of fault-bend folding, Am. J. Sci. 283, 684–721, doi: 10.2475/ajs.283.7.684.
- Takao, M., K. Ueda, T. Yasunaka, T. Kurita, H. Nakase, T. Kyotani, and J. Kato (2014). Improving the reliability of stochastic fault displacement hazard analysis, *Proc. Jpn. Assoc. Earthq. Eng.* 14, no. 2, 67–83.
- Wang, Y., and C. Goulet (2021). Validation of fault displacements from dynamic rupture simulations against the observations from the 1992 Landers earthquake, *Bull. Seismol. Soc. Am.* **111**, no. 5, 2574–2594, doi: 10.1785/0120210082.
- Wells, D. L., and K. J. Coppersmith (1994). New empirical relationships among magnitude, rupture length, rupture width, rupture area, and surface displacement, *Bull. Seismol. Soc. Am.* 84, no. 4, 974–1002.
- Wesnousky, S. G. (2008). Displacement and geometrical characteristics of earthquake surface ruptures: Issues and implications for seismic-hazard analysis and the process of earthquake rupture, *Bull. Seismol. Soc. Am.* **98**, no. 4, 1609–1632, doi: 10.1785/0120070111.
- Xu, X., X. Wen, G. Yu, G. Chen, Y. Klinger, J. Hubbard, and J. Shaw (2009). Coseismic reverse- and oblique-slip surface faulting generated by the 2008 Mw 7.9 Wenchuan earthquake, China, *Geology* 37, no. 6, 515–518, doi: 10.1130/G25462A.1.
- Yang, B., Y. Jiao, and S. Lei (2006). A study on the effects of microparameters on macroproperties for specimens created by bonded particles, *Eng. Comput.* (Swansea, Wales) 23, no. 6, 607–631, doi: 10.1108/02644400610680333.
- Yeats, R. S., K. E. Sieh, and C. R. Allen (1997). *The Geology of Earthquakes*, Oxford University Press, New York.
- Youngs, R. R., W. J. Arabasz, R. E. Anderson, A. R. Ramelli, J. P. Ake, D. B. Slemmons, J. P. McCalpin, D. I. Doser, C. J. Fridrich, F. H. Swan III, et al. (2003). A methodology for probabilistic fault displacement hazard analysis (PFDHA), Earthq. Spectra 19, no. 1, 191–219, doi: 10.1193/1.1542891.
- Yu, G., X. Xu, Y. Klinger, G. Diao, G. Chen, X. Feng, C. Li, A. Zhu, R. Yuan, T. Guo, and X. Sun (2010). Fault-scarp features and cascading-rupture model for the (Mw 7.9) Wenchuan earthquake, eastern Tibetan plateau, China, *Bull. Seismol. Soc. Am.* 100, no. 5B, 2590–2614, doi: 10.1785/0120090255.

Manuscript received 23 December 2022 Published online 26 April 2023